




Survey of the hierarchical equations of motion in tensor-train format for non-Markovian quantum dynamics

Etienne Mangaud^{1,a}, Amine Jaouadi^{2,b}, Alex Chin^{3,c}, and Michèle Desouter-Lecomte^{4,d} 

¹ MSME, Université Gustave Eiffel, UPEC, CNRS, 77454 Marne-la-Vallée, France

² LYRIDS, ECE-Paris, Graduate School of Engineering, 75015 Paris, France

³ Institut des Nanosciences de Paris, Sorbonne Université, CNRS, 75015 Paris, France

⁴ Institut de Chimie Physique UMR8000, Université Paris-Saclay, CNRS, 91405 Orsay, France

Received 5 January 2023 / Accepted 2 July 2023 / Published online 26 July 2023

© The Author(s), under exclusive licence to EDP Sciences, Springer-Verlag GmbH Germany, part of Springer Nature 2023

Abstract This work is a pedagogical survey about the hierarchical equations of motion and their implementation with the tensor-train format. These equations are a great standard in non-perturbative non-Markovian open quantum systems. They are exact for harmonic baths in the limit of relevant truncation of the hierarchy. We recall the link with the perturbative second-order time convolution equations also known as the Bloch–Redfield equations. Some theoretical tools characterizing non-Markovian dynamics such as the non-Markovianity measures or the dynamical map are also briefly discussed in the context of HEOM simulations. The main points of the tensor-train expansion are illustrated in an example with a qubit interacting with a bath described by a Lorentzian spectral density. Finally, we give three illustrative applications in which the system–bath coupling operator is similar to that of the analytical treatment. The first example revisits a model in which population-to-coherence transfer via the bath creates a long-lasting coherence between two states. The second one is devoted to the computation of stationary absorption and emission spectra. We illustrate the link between the spectral density and the Stokes shift in situations with and without nonadiabatic interaction. Finally, we simulate an excitation transfer when the spectral density is discretized by undamped modes to illustrate a situation in which the TT formulation is more efficient than the standard one.

1 Introduction

Simulating quantum dynamics of complex systems with a large number of degrees of freedom (DoF) remains a computational challenge. However, measured observables often depend on a limited number of DoFs. Thus, the full system can be described as an active subsystem embedded in an environment, which makes fluctuate the energy levels of the subsystem. The latter is often described quantum mechanically while the extended environment is treated by a wide range of possibilities based on semi-classical or quantum or statistical approaches adequately chosen with respect to the choice of system–environment partitioning. When the number of DoFs increases, standard methods become computationally untractable, which is known as the

“curse of dimensionality”. In this context, the low-rank tensor decomposition has aroused a constantly growing interest. When the surrounding is modeled by an ensemble of discrete modes, Multi Configuration Time-Dependent Hartree (MCTDH) and the multi-layer version (ML-MCTDH) [1–4] are based on tensor network algorithms, mainly the Tucker and hierarchical Tucker tensors [5, 6]. Similarly, the expression of the time-dependent multi-mode wave functions in Matrix Product State (MPS) also called Tensor-Train (TT) [7–10] expansion has revealed its efficiency in many applications [11–20].

In the usual approach of open quantum systems based on statistical mechanics with a surrounding at thermal equilibrium, the environment is described less explicitly and the active system is treated by a reduced density matrix by tracing over the bath degrees of freedom. Path integrals derived from the Feynman–Vernon influence functional [21] and the hierarchical equations of motion (HEOM) [22–24] are a priori exact methods for harmonic baths and are closely related

^a e-mail: etienne.mangaud@univ-eiffel.fr

^b e-mail: ajaouadi@ece.fr

^c e-mail: alex.chin@insp.upmc.fr

^d e-mail: michele.desouter-lecomte@universite-paris-saclay.fr
(corresponding author)

[25, 26]. HEOM may also be derived from the Nakajima–Zwanzig [27, 28] partition of the Liouville equation using the cumulant expansion of the reduced propagator and properties of the Gaussian distribution of the bath linked to the harmonic approximation [29]. Both Path Integral and HEOM formalisms have also been recently treated by the tensor formalism in the Tensor Network Path Integral [30] and in the MPS [31–34] or Tucker and hierarchical Tucker tensor format for HEOM [35]. HEOM has been applied to describe many physico-chemical processes (see the recent review by Tanimura [24]), for instance, excitation transfer in photosynthetic complexes [29, 36–40] or in other devices [41], non-adiabatic interactions and electron transfer [42–44], dynamics via conical intersections [45–50], proton transfer [51], laser optimal control [50, 52], non-equilibrium fluxes [53–55], and non-linear spectroscopies [24, 56–58].

It is worth noting that accounting for temperature is handled in a similar way in the HEOM system of equations with discrete undamped modes [59] and in a recent MPS implementation with wave functions [60] in the context of T-TEDOPA formalism [61]. In the latter, the wave function approach uses discrete vibrational bath transformed into a chain and introduces finite temperature by sampling two baths representing absorption and emission, respectively, with the latter being described by a bath of oscillators with negative frequencies. Emission into the vacuum of these negative modes mimics the absorption of environmental quanta that would be present in a physical (mixed-state) thermal bath, allowing a pure wavefunction description to capture the physics of a mixed-state initial condition without the need for thermal sampling [60, 61]. On the other hand, the particular implementation of HEOM with undamped discrete modes also samples baths with positive and negative frequencies [59]. By comparing these methods, we also emphasize that even if the reduced density matrix in open quantum systems is obtained by tracing over the bath modes, this does not mean that the information about the environment disappears. Relevant information about the baths may be extracted, for instance, the time-dependent distribution of the collective bath modes in each electronic state, which may be seen as the square modulus of a dissipative wave packet [48, 59, 62, 63] or projection of the coherence among electronic states along the collective modes [48] and fluxes [54].

In this work, we present a pedagogical survey about HEOM and their implementation with the TT format. We recall the main lines and in particular the link with the perturbative second-order time convolution equations also known as the Bloch–Redfield equations, which are an illuminating step to understand the complicated structure of HEOM. We briefly discuss how HEOM may be used to compute some theoretical tools (non-Markovianity measure or dynamical map) related to non-Markovian dynamics. We then present the principal points of the TT expansion by giving the expressions related to a simple example where a qubit interacts with a bath. Finally, we give three applications

based on models in which the system–bath coupling operator is similar to the one used in the survey. Finally, the appendix explains how to encode the main expressions with a Python package.

2 Open quantum systems and HEOM

The standard starting point in open quantum system [64–66] is the partition of the DoFs of the full complex system. The active subsystem may be only electronic DoFs like in the usual spin-boson model or include some Brownian coordinates coupled to residual baths [43, 45, 67, 68]. The generic partitioning of the full Hamiltonian in three parts is written as:

$$H = H_S + H_{SB} + H_B, \quad (1)$$

where H_S and H_B are the Hamiltonians of the active system and of the vibrational or phonon bath(s) respectively. The system Hamiltonian may be time dependent if it contains interaction with external fields. When the system interacts with N_{bath} , the system–bath coupling is $H_{SB} = \sum_{\alpha=1}^{N_{\text{bath}}} S_{\alpha} B_{\alpha}$. S_{α} and B_{α} are operators in the space of the system and in the complementary space, respectively.

In the electronic-nuclear partition, the system operators S_{α} are $n \times n$ matrices with n the number of electronic states. They act as projectors on some states when the baths tune the electronic energies (i.e., are diagonally coupled) or transition matrices between some of them when the baths make fluctuate the off-diagonal electronic coupling such as in the case of conical intersections [46–50]. In other system–bath partition cases, the system operators are the Brownian coordinates included in the active subspace [43, 45, 67, 68]. Furthermore, each bath operator B_{α} is a linear combination of the position operators q_j of the oscillators $B_{\alpha} = \sum_j^{N_{\alpha}} c_j^{(\alpha)} q_j$ in the discrete bath representation with N oscillators. The expression of the coupling coefficients $c_j^{(\alpha)}$ depends on the partition and on the choice of the coordinates. In the following, we adopt mass-weighted coordinates and the electronic-nuclear partition.

The initial total density operator $\rho_{\text{tot}}(0) = \rho_S(0) \otimes \rho_{B,\text{eq}}$ is assumed to be factorized and is the product of the system density operator $\rho_S(0)$ and a thermally equilibrated bath density operator $\rho_{B,\text{eq}} = e^{-\beta H_B} / \text{Tr}_B [e^{-\beta H_B}]$ where $\beta = 1/k_B T$ is the Boltzmann factor. Extension to correlated initial conditions has been proposed in Refs. [69–72].

2.1 Second-order auxiliary operators

It is very instructive to first examine the non-Markovian perturbative equations, which contain all the crucial tools occurring in HEOM. To do so, we consider the simplest case with only one bath, i.e., $H_{SB} = SB$.

The exact formal Nakajima–Zwanzig equation given the evolution of the reduced density matrix $\rho_S(t) = -\frac{i}{\hbar} \text{Tr}_B[H, \rho_{\text{tot}}(t)]$ may be written as:

$$\dot{\rho}_S(t) = L_S \rho_S(t) + \int_0^t K(t, \tau) \rho_S(\tau) d\tau + I(t) \quad (2)$$

with $L_S = -i[H_S, \cdot]$ the system Liouvillian and $\hbar = 1$. $K(t, \tau)$ is the memory kernel which embeds the bath influence on the system and $I(t)$ is an initial correlation term which cancels when the system and bath can be initially factorized (i.e., $I(t) = 0$ when $\rho_{\text{tot}}(0) = \rho_S \otimes \rho_{B, \text{eq}}$).

At the second order in the H_{SB} coupling, the memory kernel becomes [73]:

$$\begin{aligned} \int_0^t d\tau K(t, \tau) \rho_S(\tau) &= \int_0^t d\tau K^{(2)}(t, \tau) \rho_S(\tau) \\ &= i \int_0^t d\tau \left[S, \left\{ iC(t-\tau) U_S(t-\tau) S \rho_S(\tau) \right. \right. \\ &\quad \left. \left. \times U_S^\dagger(t-\tau) \right\} + \{hc\} \right], \end{aligned} \quad (3)$$

where $C(t)$ is the correlation function of the collective bath mode $C(t) = \langle B(t)B(0) \rangle_{\text{eq}}$, $B(t)$ is the Heisenberg representation of the operator with Hamiltonian H_B and $\langle \cdot \rangle_{\text{eq}}$ denotes the average over a Boltzmann distribution at a given temperature T . $U_S(t) = e^{-iH_S t}$ is the propagator of the system. The treatment up to the fourth order may be found in Ref. [74] and the extension by the generalized master equation method in Ref. [75].

The quantum bath correlation function is the main descriptor of the bath [76]. The usual step to go towards the second order auxiliary density operator (ADO) or HEOM is the representation of the correlation function as a sum of damped decaying functions:

$$C(t-\tau) = \langle B(t)B(\tau) \rangle_{\text{eq}} = \sum_{k=1}^K \alpha_k e^{i\gamma_k(t-\tau)}, \quad (4)$$

where α_k and γ_k are complex parameters. The sum is a priori infinite but truncated to K modes, which have been called the ‘‘artificial bath modes’’ in Ref. [73]. Some extensions to different analytical forms or arbitrary correlation functions have been proposed recently in Refs. [77–81].

By inserting Eq. (4) in Eqs. (2) and (3), each artificial mode corresponds to a particular memory integral of the time-dependent integro-differential equation. Each integral is set equal to an ADO:

$$\begin{aligned} \rho_k(t)/(i\alpha_k) &= \int_0^t d\tau \left[S, \left\{ i e^{-\gamma_k(t-\tau)} U_S(t-\tau) S \rho_S(\tau) \right. \right. \\ &\quad \left. \left. \times U_S^\dagger(t-\tau) \right\} + \{hc\} \right]. \end{aligned} \quad (5)$$

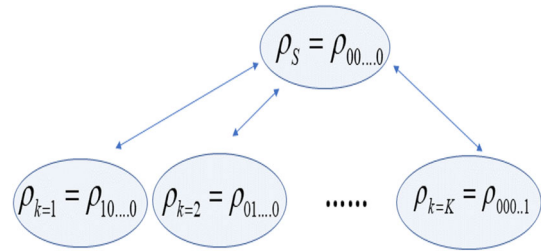


Fig. 1 Schematic representation of the auxiliary operators associated with each artificial bath mode $k = 1, K$ and involved in the second-order master equation (Eq. (6)). Each ADO corresponds to a single excitation in the mode

The dimension of $\rho_k(t)$ is that of the S operator and thus of H_S . A time local system of coupled equations may be obtained by taking the first derivative [69, 73, 82]. Different choices are possible to define the ADOs. From Eq. (5), we obtain the operational equations [69]:

$$\begin{aligned} \dot{\rho}_S(t) &= L_S \rho_S(t) + i \sum_{k=1}^K [S, \rho_k(t)] \\ \dot{\rho}_k(t) &= (i\gamma_k + L_S) \rho_k(t) + i[\alpha_k S \rho_S(t) \\ &\quad - \tilde{\alpha}_k \rho_S(t) S], \end{aligned} \quad (6)$$

where L_S is the system Liouvillian. The $\tilde{\alpha}_k$ parameters will be discussed below.

Each ADO being associated only with one decay mode, it may be considered as resulting from a single excitation in this mode and denoted by an array of K indexes with one in the k th position and zero everywhere else as shown in Fig. 1. These ADOs will constitute the first level of the HEOM hierarchy.

A real classical correlation function may be obtained by molecular dynamics [15, 38, 44, 83] or directly from experimental results [84] and corrected to get the complex quantum correlation function satisfying the fluctuation-dissipation theorem [76]. Direct parametrization of $C(t)$ fitted by different approaches [81], Prony method [80] or expansion on Chebyshev or Bessel functions [77] have also been proposed. However, the relation with the bath spectral density, defined as follows:

$$C(t) = \int_{-\infty}^{\infty} d\omega J(\omega) (e^{\beta\omega} - 1)^{-1} e^{-i\omega t}, \quad (7)$$

where $\beta = 1/k_B T$ is the Boltzmann factor, is currently used and the $\{\alpha_k, \gamma_k\}$ parameters are obtained from the parametrization of $C(\omega) = J(\omega) (e^{\beta\omega} - 1)^{-1}$, where $J(\omega)$ is independent of the temperature and $(e^{\beta\omega} - 1)^{-1}$ is the Bose function related to the quantum fluctuation–dissipation theorem. In the discrete case, the spectral density is defined from the system–bath

coupling coefficients c_j related to N_{disc} discrete modes

$$J(\omega) = \frac{\pi}{2} \sum_{j=1}^{N_{\text{disc}}} \frac{c_j^2}{\omega_j} \delta(\omega - \omega_j). \quad (8)$$

In the continuous representation, the spectral density is often approximated by an Ohmic function $J_{\text{Ohm}} \approx c\omega f_{\text{cutoff}}(\omega)$ or a super-Ohmic function $J_{\text{SuperOhm}} \approx c\omega^3 f_{\text{cutoff}}(\omega)$, with c a constant and f_{cutoff} an exponential or Lorentzian cutoff. The Ohmic function is used for solvents, while the super-Ohmic one is relevant for the solid phase and phonon baths. To get a parametrization of the bath correlation function (Eq. (4)) through Eq. (7), one has to perform a fitting procedure of the spectral functions with relevant analytical functions. A special care in fitting the spectral density low frequency behavior is often necessary to get accurate results [85]. Here, we will discuss only the cases of Ohmic and super-Ohmic Lorentzian functions. We adopt the Tannor–Meier parametrization [73] in which the spectral density is fitted by n_{lor} two-pole Lorentzian functions depending on three parameters $(p_l, \Omega_l, \Gamma_l)$ where p_l is the associated weight, Ω_l the central frequency, and Γ_l the bandwidth.

$$J_{\text{Ohm}}(\omega) = \sum_{l=1}^{n_{\text{lor}}} \frac{p_l \omega}{\Upsilon(\Omega_l, \Gamma_l)} \quad (9)$$

with

$$\Upsilon(\Omega_l, \Gamma_l) = [(\omega + \Omega_l)^2 + \Gamma_l^2][(\omega - \Omega_l)^2 + \Gamma_l^2].$$

All the $\{\alpha_k, \gamma_k\}$ parameters may be obtained from the integral (7) after substitution of Eq. (9). Each Lorentzian corresponds to two artificial decay modes. The Bose function generates an infinite series of terms coming from its poles. They are known as the Matsubara terms. In practice, the number of Matsubara terms is very small at high temperature but may become numerous at low temperature rendering the ADO method computationally more demanding. In the low-temperature regime, Padé approximants of the Bose function [86], fitting procedure of $C(t)$ used to capture the Matsubara terms [87] or a recent correction scheme [88] can be used. The analytical expressions of $\{\alpha_k, \gamma_k\}$ (Eq. (4)) as functions of the $(p_l, \Omega_l, \Gamma_l)$ parameters of $J_{\text{Ohm}}(\omega)$ and those related to the Matsubara terms are given in Refs. [69] or [67]. One also could find in these references the expression of the $\tilde{\alpha}_k$ parameters (see Eq. (6)). They come from a particular expression of the complex conjugate of $C(t)$ that may be written as: $C^*(t) = \sum_{k=1}^K \tilde{\alpha}_k e^{i\gamma_k t}$ with the same γ_k as in Eq. (4). In the super-Ohmic case, the fitting functions have four poles leading to four artificial decay

channels

$$J_{\text{SuperOhm}}(\omega) = \sum_{l=1}^{n_{\text{lor}}} \frac{p_l \omega^3}{\Upsilon(\Omega_{l,1}, \Gamma_{l,1}) \Upsilon(\Omega_{l,2}, \Gamma_{l,2})}. \quad (10)$$

The analytical expressions to get the $\{\alpha_k, \gamma_k\}$ parameters of $C(t)$ (Eq. (4)) from $(p_l, \Omega_{l,1}, \Gamma_{l,1}, \Omega_{l,2}, \Gamma_{l,2})$ parameters of $J_{\text{SuperOhm}}(\omega)$ are gathered in Ref. [89].

2.2 HEOM

First, we discuss the case with a single bath, i.e., we consider only one S operator. The generalization will be discussed at the end of the section. When the bath correlation time becomes long with respect to the system characteristic timescale due to a strongly peaked spectral density, the high non-Markovianity generally involves a non-perturbative regime. HEOM are one of the reference dynamical methods for open quantum systems modeled with a harmonic bath. The equations giving the evolution of the reduced density matrix were originally derived for a Drude–Lorentz spectral density in the high-temperature limit from the Kubo stochastic Liouville equation [22–24, 90] and the Feynman–Vernon influence functional formalism [25, 26]. Another approach to derive these equations is by referring to the remarkable property that the cumulant expansion limited to second order is exact when the bath statistics are Gaussian [29, 91]. This is based on the Wick theorem [92]. The reduced density matrix $\rho_{S,I}(t)$ for the system in interaction representation $\rho_{S,I}(t) = e^{iH_0 t} \rho_S(t) e^{-iH_0 t}$ with $H_0 = H_S + H_B$, is given by the partial trace over the bath of the time evolution of the total density matrix:

$$\rho_{S,I}(t) = \text{Tr}_B \left[\mathcal{T}^{(+)} e^{\int_0^t d\tau L_{\text{SB},I}(\tau)} \rho_B^{\text{eq}} \right] \rho_{S,I}(0), \quad (11)$$

where $\mathcal{T}^{(+)}$ is a time-ordering operator and a factorization is assumed at the initial time $t = 0$. $L_{\text{SB},I}(t)$ is the Liouvillian in interaction representation, $L_{\text{SB},I}(t) = -i[S(t)B(t), \bullet]$, where $S(t) = e^{iH_S t} S e^{-iH_S t}$ and $B(t) = e^{iH_B t} B e^{-iH_B t}$.

At the second order in the cumulant expansion, Eq. (11) becomes

$$\rho_{S,I}(t) = \mathcal{T}^{(+)} e^{\int_0^t d\tau \mathcal{K}_I(\tau)} \rho_{S,I}(0). \quad (12)$$

$\mathcal{K}_I(\tau) = \int_0^\tau dt' K_I^{(2)}(\tau, t')$ corresponds to the second-order memory term occurring in the second-order perturbation theory (Eq. (3)) but here, the second order is an exact expression for the cumulant expansion:

$$\int_0^\tau dt' K_I^{(2)}(\tau, t') \cdot = -[S(\tau), \int_0^\tau dt' C(\tau - t') S(t') \cdot - \{h.c.\}]. \quad (13)$$

By inserting the correlation function parametrization (Eq. (4)), Eq. (13) is separable into a sum of K operators \mathcal{K}_{Ik} where K is the number of artificial decay modes. In addition, each \mathcal{K}_{Ik} is decomposed as:

$$\mathcal{K}_{Ik}(\tau) = \Phi_I(\tau) W_{Ik}(\tau), \quad (14)$$

where

$$\Phi_I(\tau) \cdot = -[S(\tau), \cdot] \quad (15)$$

and

$$W_{Ik}(\tau) = \int_0^\tau dt' e^{i\gamma_k(\tau-t')} \Theta_{Ik}(t') \quad (16)$$

with

$$\Theta_{Ik}(t') \cdot = \alpha_k S(t') \cdot - \tilde{\alpha}_k \cdot S(t'). \quad (17)$$

The exact solution takes the following form:

$$\begin{aligned} \rho_{S,I}(t) &= \mathcal{T}^{(+)} \prod_k^K e^{\int_0^t d\tau \mathcal{K}_{Ik}(\tau)} \rho_{S,I}(0) \\ &= \mathcal{T}^{(+)} \prod_k^K e^{\int_0^t d\tau \int_0^\tau dt' \Phi_I(t') e^{i\gamma_k(\tau-t')} \Theta_{Ik}(t')} \\ &\quad \times \rho_{S,I}(0). \end{aligned} \quad (18)$$

The master equation can then be derived as

$$\dot{\rho}_{S,I}(t) = \mathcal{T}^{(+)} \sum_k^K \mathcal{K}_{Ik}(t) \rho_{S,I}(t). \quad (19)$$

This equation is time non-local since $\mathcal{K}_{Ik}(t)$ contains an integral. A time local system of coupled equations is obtained by defining the ADOs by the same strategy as in the second order approach:

$$\rho_{\mathbf{n},I}(t) = \mathcal{T}^{(+)} \prod_k^K W_{Ik}(t)^{n_k} e^{\int_0^t d\tau \mathcal{K}_{Ik}(\tau)} \rho_{S,I}(0), \quad (20)$$

where

$$\mathbf{n} = \{n_1, \dots, n_k, \dots, n_K\} \quad (21)$$

in a vector of nonnegative integers giving the occupation number in each artificial decay mode. The case $\mathbf{n} = \{0, \dots, 0, \dots, 0\}$ corresponds to $\rho_{S,I}$. Time local coupled equations among the ADOs may be derived by working with the Fourier–Laplace transforms of

Eqs. (18) and (20) and using integration by parts [36, 48]. One recovers the relations established in Ref. [22]. After the inverse Laplace–Fourier transform and the return in the Schrödinger representation, the HEOM read:

$$\begin{aligned} \dot{\rho}_{\mathbf{n}}(t) &= L_S \rho_{\mathbf{n}}(t) + i \sum_{k=1}^K n_k \gamma_k \rho_{\mathbf{n}}(t) \\ &\quad - i \left[S, \sum_{k=1}^K \rho_{\mathbf{n}_k^+}(t) \right] \\ &\quad - i \sum_{k=1}^K n_k \left(\alpha_k S \rho_{\mathbf{n}_k^-}(t) - \tilde{\alpha}_k \rho_{\mathbf{n}_k^-}(t) S \right) \end{aligned} \quad (22)$$

or more shortly using definitions (15) and (17) in Schrödinger representation (i.e., $\Phi(\tau) \cdot = -[S, \cdot]$ and $\Theta_{k\cdot} = \alpha_k S \cdot - \tilde{\alpha}_k \cdot S$):

$$\begin{aligned} \dot{\rho}_{\mathbf{n}}(t) &= L_S \rho_{\mathbf{n}} \\ &\quad + i \sum_{k=1}^K \left(n_k \gamma_k \rho_{\mathbf{n}} - \Phi \rho_{\mathbf{n}_k^+} - n_k \Theta_k \rho_{\mathbf{n}_k^-} \right). \end{aligned} \quad (23)$$

The subscripts

$$\mathbf{n}_k^+ = \{n_1, \dots, n_k + 1, \dots, n_{n_K}\}$$

and

$$\mathbf{n}_k^- = \{n_1, \dots, n_k - 1, \dots, n_{n_K}\}$$

denote the matrices for which one occupation number differs by one unit in the hierarchy $n_k \rightarrow n_k \pm 1$. The sum of the occupation numbers defines the level of the hierarchy $L = \sum n_k$. The total number of matrices when the hierarchy is limited at level L is $(L+K)!/L!K!$. Each matrix is connected to the matrices of the lower or the upper levels. Figure 2 illustrates the case with two artificial decay channels (i.e., one Ohmic Lorentzian in the spectral density and no Matsubara term). Initially, $\rho_{00\dots 0} = \rho_S$ and all the ADOs are zero. They represent the initial bath at equilibrium. When the final relaxed state is reached, the converged ADOs represent the new equilibrium and may be taken as the initial condition to describe another process affecting the equilibrated system. For instance to describe the stationary fluorescence. All the terms occurring in the derivative of each ADO are schematized in Fig. 2 for a simple example with two bath modes.

The generalization is straightforward when there are N_{bath} uncorrelated baths, each associated with K_b artificial bath modes. Then, $K = \sum_{b=1}^{N_{\text{bath}}} K_b$. Each bath is linked to the system by an operator S_b and the equations become:

$$\begin{aligned} \dot{\rho}_{\mathbf{n}}(t) &= L_S \rho_{\mathbf{n}} + i \sum_b^{N_{\text{bath}}} \sum_{k=1}^{K_b} \left(n_{b,k} \gamma_{b,k} \rho_{\mathbf{n}} \right. \\ &\quad \left. - \Phi_b \rho_{\mathbf{n}_k^+} - n_{b,k} \Theta_{b,k} \rho_{\mathbf{n}_k^-} \right). \end{aligned} \quad (24)$$

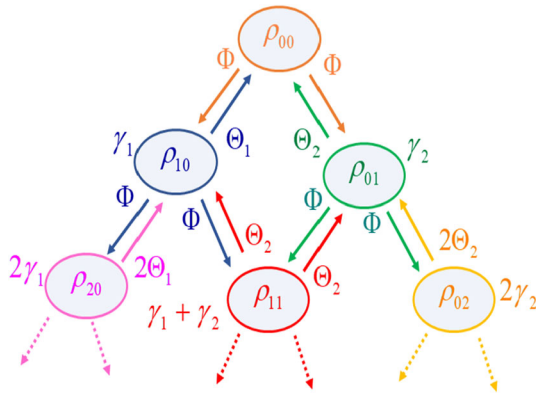


Fig. 2 Schematic representation of the auxiliary operators of the HEOM hierarchy up to level $L = 2$ for the case with two artificial bath modes $K = 2$. Φ acts on matrices for which one occupation number increases by one unit. Θ_k is applied on matrices for which one occupation number decreases by one unit. The sum of the decay rates $n_k \gamma_k$ multiplying each matrix is indicated. The schematic representation of the terms involved in the derivative of one matrix is complete for ρ_{00} (orange); ρ_{10} (blue) and ρ_{01} (green)

An alternative to the continuous representation of the spectral density with K artificial modes is the discretization with N_{disc} undamped modes in the spirit of MCTDH or ML-MCTDH computations [93–96] or MPS simulations in the Hilbert space [12–15]. Discretization has also been illustrated with HEOM [59] and checked in TT format [31, 35]. The expression of the corresponding HEOM equations are given in Refs. [31, 59]. The active system is then coupled to two identical baths with positive or negative frequencies describing emission and absorption of energy. Since there are two baths, the number of terms in the correlation function is large $K = 2N_{\text{disc}}$ but there are no Matsubara terms associated with the poles of the Bose function in the continuous case. The discrete couplings are smaller than those of the artificial modes. We will illustrate in one application that the TT implementation may be more efficient than the standard one in that case.

The system of the coupled differential equations (24) or those related to discrete modes given in Refs. [31, 59] can then be solved using standard numerical methods such as Runge–Kutta 4 (RK4), Cash–Karp (RK4-5) adaptive step-size or Arnoldi algorithms. Although HEOM are an infinite system of differential equations, they are truncated at a maximum value of $n_k = n_{\text{max}}$. Thus, several simulations with increasing values of n_{max} should be carried out until the results (density matrix or observables) are properly converged. For comparison between the standard and TT formulations, we have used a home-made fortran code parallelized with OpenMP. Other implementations in python or on new architectures such as GPU [97] could be useful. See a review of different software in Ref. [81].

2.3 HEOM and non-Markovianity

As mentioned above, HEOM are a standard method to tackle non-perturbative and non-Markovian regimes. Non-Markovianity obviously depends on the partition since it is roughly predicted by the characteristic timescales of the active system and the corresponding bath. These typical dynamical times may be very different with respect to the system definition. Inserting some effective bath coordinates into the system part (to reduce the coupling towards the residual bath and modify the corresponding timescales) may be an efficient strategy to change the Markovianity regime [43, 48, 67, 68, 98, 99]. When the partition leads to a non-Markovian regime, an abundant literature has been devoted to the characterization of the non-Markovianity by different measures and from a fundamental perspective, to a mathematical definition of non-Markovian quantum dynamical maps, which is still an open problem. These fundamental questions are reviewed for instance in Refs. [100, 101]. A detailed presentation of these items is beyond the scope of this paper and we summarize here only the main points. A Markovian behavior is linked to a continuous loss of information from the open system to the surrounding while a flow from the environment back to the open system is the signature of a non-Markovian effect. The return of information from the bath could modify the system dynamics. The measures aim at quantifying this backward flow. One may cite, among others, the trace distance measure [100, 102], the entanglement measure [103], negativity of time-dependent canonical rates [104], and the Bloch volume measure [105]. They are compared for instance in Refs. [104, 106]. In the last case, the measure is based on an estimation of the volume of the accessible states in the generalized Bloch sphere for a n -state system. A non-monotonic decrease of this volume is a signature of non-Markovianity. Any density matrix may be expanded in the basis set of n^2 operators: the normalized identity $G_0 = I/\sqrt{n}$ and $G_i (i = 1, \dots, n^2 - 1)$: the $n^2 - 1$ generators of $SU(n)$ [107, 108]. They are the Pauli matrices for $n = 2$ and the Gell-Mann matrices for $n = 3$. The volume of accessible states $V(t) = \det(\mathbf{F}(t))$ is obtained from the determinant of the matrix $F_{m,n}(t) = \text{Tr}(G_m(0)G_n(t))$. This requires n^2 propagations of the basis operators and is easily obtained with HEOM [48, 52, 63, 89, 109, 110]. Similarly, the n^2 basis operators may be used to build the $n^2 \times n^2$ decoherence matrix [89, 104] $D_{ij}(t) = \sum_{m=0}^{n^2-1} \text{Tr}[G_m G_i \Lambda_t[G_m(t)] G_j]$, where $\Lambda_t[G_m(t)]$ is the map of the time local equation $\dot{G}_m(t) = \Lambda_t[G_m(t)] = \sum_{k=0}^{n^2-1} \dot{\phi}_t[G_k] F(t)_{km}^{-1} \cdot \dot{\phi}_t[G_k]$ is the derivative of the system density matrix when the initial state is G_k (see Eq. (22)). The eigenvalues of this decoherence matrix are called the canonical decay rates $\gamma_k(t)$ [89, 104]. They witness non-Markovianity when some of them become negative signaling an information return towards the system.

The concept of dynamical map in the theory of open quantum systems is relevant when the initial state of

the total system is a factorized product state but it remains a debated point for initial system–bath entangled state [100, 111, 112]. While the master equation is related to the time derivative $\dot{\rho}(t) = \Lambda_t[\rho(t)]$, the corresponding dynamical map ϕ_t transformed any initial state $\rho(0)$ to $\rho(t)$, i.e., $\rho(t) = \phi_t[\rho(0)]$. The map is expected to be completely positive or at least positive to ensure that ϕ_t maps physical states to physical states. This preserves the Hermiticity and the trace of operators. The mathematical properties of the map are discussed mainly in the quantum information community. By expanding both $\phi_t[\rho(0)]$ and $\rho(0)$ in the basis of the n^2 operators G_k , the map may be expressed in matrix notation $\rho(t) = \sum_{k,l=0}^{n^2-1} F_{lk}(t) \text{Tr}[G_l \rho(0)] G_k$, i.e., as a function of the $\mathbf{F}(t)$ matrix discussed above and easily computed by HEOM. To analyze the positivity, it is rather the $n^2 \times n^2$ Choi matrix [104, 113, 114] that is used. It corresponds to the expansion of the map in the basis set of the n^2 projector matrices $|j\rangle\langle k|$ related to a basis of the system Hilbert space in place of the generators G_n . The map is completely positive if and only if the eigenvalues of the Choi matrix are positive. This Choi matrix would be easily obtained by HEOM by a procedure similar to that providing the $\mathbf{F}(t)$ matrix via the propagation of the n^2 projector matrices $|j\rangle\langle k|$. To our knowledge, this systematic analysis has not been carried out with HEOM and could be interesting. In our previous works, we have mainly computed with HEOM $\mathbf{F}(t)$ [109, 110] and the canonical rates $\gamma_k(t)$ [52, 89]. Anyhow, we did not detect a loss of conservation of the trace of $\rho_S(t)$ even when dynamics is non-Markovian as shown by the volume of accessible states or by the canonical rates. It is well known that numerical instabilities with non-conservation of the norm may occur mainly for long time in the standard formulation of HEOM [115] or in the TT approach due to the variational approach [32] and limitation of the tensor ranks [33].

The control of open quantum systems [116] has aroused a renewed interest mainly in the context of quantum technologies that rely on the coherent manipulation and transfer of information, encoded in quantum states [117–119]. Non-Markovianity is expected to be a resource to improve the control by exploiting the transitory flow back. The HEOM formalism has proven its efficiency when it is coupled with different control strategies, in particular with optimal control protocols [50, 52].

3 HEOM in tensor-train format

In this section, we summarize the main relations of the tensor-train formalism (also named matrix product state (MPS)) that is an interesting way for representing a high-dimensional tensor as the one we are using for HEOM. The idea of this TT format is to decompose the tensor into a network of low-dimensional tensors called

TT cores coupled in a chain. MPS has received a growing interest in the quantum physics community [11–20]. The application in HEOM was already suggested by Shi [31, 32] who also uses the Tucker representation [35] and later by Borelli [33, 34]. We present a pedagogical survey showing the way the super-operators involved in the TT-HEOM formalism are written and by expliciting them in a simple case of a two-level system coupled to a bath with a spectral density fitted by an Ohmic Lorentzian (Eq. (9)) leading to two artificial decay modes. The Appendix gathers the main steps for the encoding in python.

3.1 Representation of the ADOs

When the system is a n -state case, each ADO is a $n \times n$ matrix that may be reshaped in a super-vector with n^2 elements $\bar{\rho}_{\mathbf{n}}^{\alpha}$, where $\alpha \in [1, n^2]$ stands for a (a, b) element of the system density matrix ($a, b \in [1, n]$). The global index \mathbf{n} corresponds as in Eq. (21) to the occupation number in each decay mode. When the TT format is adopted, each occupation number n_k runs from 0 to n_{\max} . The total number of matrices is then larger than when the hierarchy is truncated at a given level L in the standard formulation. Each element of the high-dimensional array $\bar{\rho}$ is written in TT format as:

$$\begin{aligned} \bar{\rho}_{\mathbf{n}}^{\alpha} \approx & \sum_{j_0} \sum_{j_1} \cdots \sum_{j_k} \cdots \sum_{j_{K+1}} A_0(j_0, \alpha, j_1) \\ & \times A_1(j_1, n_1, j_2) \cdots A_k(j_k, n_k, j_{k+1}) \\ & \times \cdots A_K(j_K, n_K, j_{K+1}). \end{aligned} \quad (25)$$

The summation index j_k goes from 1 to r_k , where r_k is the rank also called the bond ($r_0 = r_{K+1} = 1$ for dimensionality consistency). K is the number of decay modes. A_k are the cores, i.e., arrays of dimension $r_k \times n_{\text{dim}} \times r_{k+1}$, where $n_{\text{dim}} = n^2$ for $k = 0$ and $n_{\text{dim}} = n_{\text{HEOM}} = n_{\max} + 1$ for $k \neq 0$ ($n_{\text{HEOM}} = L + 1$, where L is the hierarchy level). The choice of the rank r_k is crucial and convergence must be carefully checked. Complex baths (and realistic ones) often need many decay modes and high hierarchy level: K and L increase dramatically which leads to heavy simulations.

TT decomposition allows a priori to deal with this dimensionality curse. Indeed, instead of using an array with $n^2 \times n_{\text{HEOM}}^K$ in a standard approach, the tensor-train decomposition stores $n^2 r_1 \times n_{\text{HEOM}} \prod_{k=1}^K r_k r_{k+1}$ tensor elements. For instance, if the ranks for every core are all the same ($\forall k \in [1, K], r_k = r$), the number of elements is $r(n^2 + n_{\text{HEOM}}) + Kr^2 n_{\text{HEOM}}$ in the TT approach. With the TT formalism, the increase with the number of modes is linear with K . This might allow to deal with large values of K and thus extend the capabilities of the HEOM method to describe more complex environments. However, the TT decomposition approximates the real tensor and is exact only if the ranks r_k grow up to infinity. In practise, they are truncated to a sufficiently high value to ensure the computation convergence. Choosing the best ranks is not a trivial task

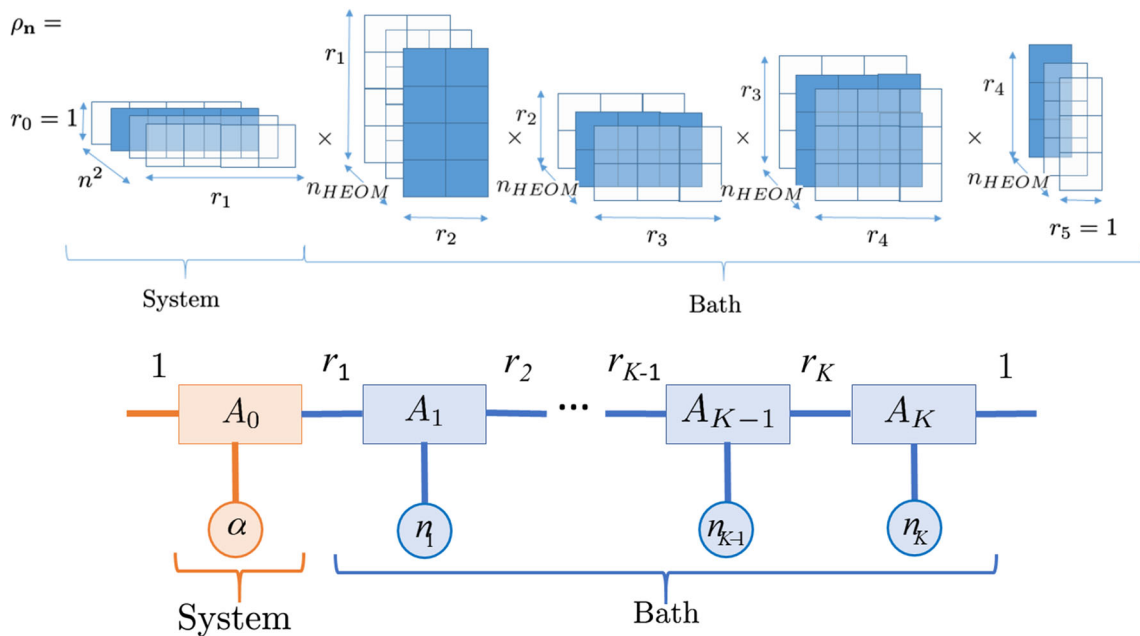


Fig. 3 Upper panel: Schematic representation of a tensor train with the HEOM formalism for a two-level system ($n = 2$) with a bath modeled by two single Tannor–Meier Lorentzian functions with no Matsubara frequencies ($K = 4$) at a hierarchy level of $n_{HEOM} = 3$. Individual matrices or vectors are called cores of the tensor (and often denoted as A_k). Arbitrary values have been chosen here for the tensor ranks: $r_1 = 4, r_2 = 2, r_3 = 3$ and $r_4 = 4$. For instance, the tensor element $\rho_{2,3,2,2,1}$, which corresponds to $\rho_{3,2,2,1}^{12}$, i.e., the element 1,2 of the ADO for occupation number $\mathbf{n} = 3, 2, 2, 1$, is computed by performing vector–matrix, matrix–matrix or matrix–vector products with the blue cores on the figure. As the initial and final tensor ranks ($r_0 = r_{K+1} = 1$) are equal to one, the final result is a scalar number. Lower panel: Tensor-train representation of the ADOs. A_k are the cores of the tensor. The circles represent the physical legs. α runs from 1 to n^2 , where n is the number of states in the system and n_k is the index (occupation number) for each decay mode that runs from 0 to n_{max} . The rectangles are matrices $r_{k-1} \times r_k$, where the rank r_k is also called the bond

and goes beyond the scope of this article. We discuss this point in Sect. 3.3.

Tensor representations are schematized in Fig. 3.

3.2 HEOM super-Liouvillian

The HEOM equations (23) and (24) contain a Liouvillian operator related to the Hamiltonian of the system, a damping term, a term coupling to matrices of a higher level in the hierarchy and a term coupling to a lower level. In super-operator notation, one has:

$$\mathcal{L} = \mathcal{L}_S + \sum_{k'=1}^K (\mathcal{L}_{k'} + \mathcal{L}_{k'+} + \mathcal{L}_{k'-}), \quad (26)$$

where $k' = (k, b)$ is a collective index which addresses both the index of the correlation function terms ($k \in [1, n_{cor}, b]$) and the bath b .

For pedagogical purpose, in this section, we give the expression of the different contributions to the super-operator of the forward propagation with TT for a simple example. We consider a two-level system ($n = 2$). The excited state is coupled to a single bath that tunes the energies and is coupled diagonally to the system. The spectral density is a two-pole Lorentzian leading to

two decay modes ($K = 2$). We assume a high temperature, so there is no Matsubara term. The corresponding coupling operator is

$$S_k = \begin{pmatrix} 0 & 0 \\ 0 & 1 \end{pmatrix} \quad (27)$$

for decay mode $k = 1, 2$. HEOM is treated at order two $n_{HEOM} = 2$, i.e., for each mode, the occupation number n_k may take the value 0 or 1 ($n_{max} = 1$). The hierarchy contains 4 (2×2) matrices related to occupation numbers 00, 01, 10, and 11. The super-operator is then a (16×16) matrix in this example.

All the elements of all the ADOs ($n \times n$ matrices) are reshaped in a super-vector that contains n^2 groups corresponding to a given element of the system density matrix $\alpha = (a, b)$ when the ADO indexes of $\{n_1, \dots, n_k, \dots, n_K\}$ run from 0 to n_{max} beginning by the last one. In the example with a two-level system, two decay modes ($K = 2$) and $n_{max} = 1$, there are 4 groups labeled 00, 01, 10, and 11 (see Fig. 4).

3.2.1 Matrix \mathcal{L}_S

The expression of the $n^2 \times n^2$ super-operator for the system Liouvillian, which must act on the system density

L_{11}		L_{12}		L_{13}		L_{14}	
L_{11}		L_{12}		L_{13}		L_{14}	
	L_{11}		L_{12}		L_{13}		L_{14}
	L_{11}		L_{12}		L_{13}		L_{14}
L_{21}		L_{22}		L_{23}		L_{24}	
L_{21}		L_{22}		L_{23}		L_{24}	
	L_{21}		L_{22}		L_{23}		L_{24}
	L_{21}		L_{22}		L_{23}		L_{24}
L_{31}		L_{32}		L_{33}		L_{34}	
L_{31}		L_{32}		L_{33}		L_{34}	
	L_{31}		L_{32}		L_{33}		L_{34}
	L_{31}		L_{32}		L_{33}		L_{34}
L_{41}		L_{42}		L_{43}		L_{44}	
L_{41}		L_{42}		L_{43}		L_{44}	
	L_{41}		L_{42}		L_{43}		L_{44}
	L_{41}		L_{42}		L_{43}		L_{44}

$\rho_{(0,0)}^{11}$
$\rho_{(0,1)}^{11}$
$\rho_{(1,0)}^{11}$
$\rho_{(1,1)}^{11}$
$\rho_{(0,0)}^{12}$
$\rho_{(0,1)}^{12}$
$\rho_{(1,0)}^{12}$
$\rho_{(1,1)}^{12}$
$\rho_{(0,0)}^{21}$
$\rho_{(0,1)}^{21}$
$\rho_{(1,0)}^{21}$
$\rho_{(1,1)}^{21}$
$\rho_{(0,0)}^{22}$
$\rho_{(0,1)}^{22}$
$\rho_{(1,0)}^{22}$
$\rho_{(1,1)}^{22}$

Fig. 4 Matrix \mathcal{L}_S (Eq. (29)). The L_{ij} elements are the concise notation for $(\mathcal{L}_{S(\text{ADO})})_{ij}$ defined in Eq. (28). The empty regions correspond to zero

matrix and on each auxiliary density operator (ADO), is straightforward (\otimes denotes here the Kronecker product):

$$\begin{aligned} \mathcal{L}_{S(\text{ADO})} &= -i(H \otimes I_n - I_n \otimes H) \\ &= -i \begin{pmatrix} 0 & -H_{12} & H_{12} & 0 \\ -H_{21} & H_{11} - H_{22} & 0 & H_{12} \\ H_{21} & 0 & H_{22} - H_{11} & -H_{12} \\ 0 & H_{21} & -H_{21} & 0 \end{pmatrix}. \end{aligned} \tag{28}$$

The expression of the super-operator \mathcal{L}_S is then

$$\mathcal{L}_S = \mathcal{L}_{S(\text{ADO})} \otimes \prod_{k''=1}^K I_{n_{\text{HEOM}}} \tag{29}$$

becoming $\mathcal{L}_S = \mathcal{L}_{S(\text{ADO})} \otimes I_2 \otimes I_2$ in the example with $K = 2$ and $n_{\text{HEOM}} = 2$. The corresponding matrix is given in Fig. 4, where we have adopted the concise notation $L_{ij} = (\mathcal{L}_{S(\text{ADO})})_{ij}$.

3.2.2 Damping Liouvillian $\mathcal{L}_{\text{damp}}$

The damping term is $\mathcal{L}_{\text{damp}} = \sum_{k'=1}^K (\mathcal{L}_{k'})$, where

$$\mathcal{L}_{k'} = i\gamma_{k'} I_{n^2} \otimes \prod_{k''=1}^K M_{k''} \tag{30}$$

with $M_{k''} = I_{n_{\text{HEOM}}}$ if $k'' \neq k'$ and $M_{k'',lm} = (l-1)\delta_{l,m}$ if $k'' = k'$ ($l, m \in [1, n_{\text{HEOM}}]$). It is diagonal in the super-operator representation. For each decay mode k' , all the elements of the matrices ρ_n are multiplied by

the decay rate $\gamma_{k'}$ times the occupation number $n_{k'}$. In the two-level and two-decay case with $n_{\text{HEOM}} = n_{\text{max}}$, one has:

$$\begin{aligned} \mathcal{L}_1 &= i\gamma_1 I_{n^2} \otimes M \otimes I_{n_{\text{NHEOM}}} \\ &= i\gamma_1 \begin{pmatrix} 1 & & & \\ & 1 & & \\ & & 1 & \\ & & & 1 \end{pmatrix} \otimes \begin{pmatrix} 0 & & & \\ & 1 & & \\ & & \ddots & \\ & & & n_{\text{max}} \end{pmatrix} \\ &\quad \otimes \begin{pmatrix} 1 & & & \\ & 1 & & \\ & & \ddots & \\ & & & 1 \end{pmatrix} \end{aligned} \tag{31}$$

and

$$\begin{aligned} \mathcal{L}_2 &= i\gamma_2 I_{n^2} \otimes I_{n_{\text{NHEOM}}} \otimes M \\ &= i\gamma_2 \begin{pmatrix} 1 & & & \\ & 1 & & \\ & & 1 & \\ & & & 1 \end{pmatrix} \otimes \begin{pmatrix} 1 & & & \\ & 1 & & \\ & & \ddots & \\ & & & 1 \end{pmatrix} \\ &\quad \otimes \begin{pmatrix} 0 & & & \\ & 1 & & \\ & & \ddots & \\ & & & n_{\text{max}} \end{pmatrix}. \end{aligned} \tag{32}$$

When $n_{\text{max}} = 1$ and, thus, $n_{\text{NHEOM}} = 2$, $M = \begin{pmatrix} 0 & \\ & 1 \end{pmatrix}$ and $I_{n_{\text{NHEOM}}} = I_2$. The corresponding $\mathcal{L}_{\text{damp}}$ matrix divided by i is given in Fig. 5.

3.2.3 Matrix \mathcal{L}_+

Each term $\mathcal{L}_{k'+}$ addressing the upper level of the hierarchy in Eqs. (23) or (24) corresponds to the super-operator

$$\mathcal{L}_{k'+} = -i(S_{k'} \otimes I_n - I_n \otimes S_{k'}) \otimes \prod_{k''=1}^K M'_{k''}, \tag{33}$$

where $M'_{k''} = I_{n_{\text{HEOM}}}$ if $k'' \neq k'$ and $M'_{k'',lm} = \delta_{l+1,m}$ if $k'' = k'$ ($l, m \in [1, n_{\text{HEOM}}]$). We consider the case with a single bath with a system–bath coupling operator S (Eq. (27)). Then, $S_{k'}$ is independent of k' . The factor $Q_+ = (S \otimes I_n - I_n \otimes S)$ in the two-state case with $n = 2$ is:

$$Q_+ = \begin{pmatrix} 0 & 0 & 0 & 0 \\ 0 & -1 & 0 & 0 \\ 0 & 0 & 1 & 0 \\ 0 & 0 & 0 & 0 \end{pmatrix}. \tag{34}$$

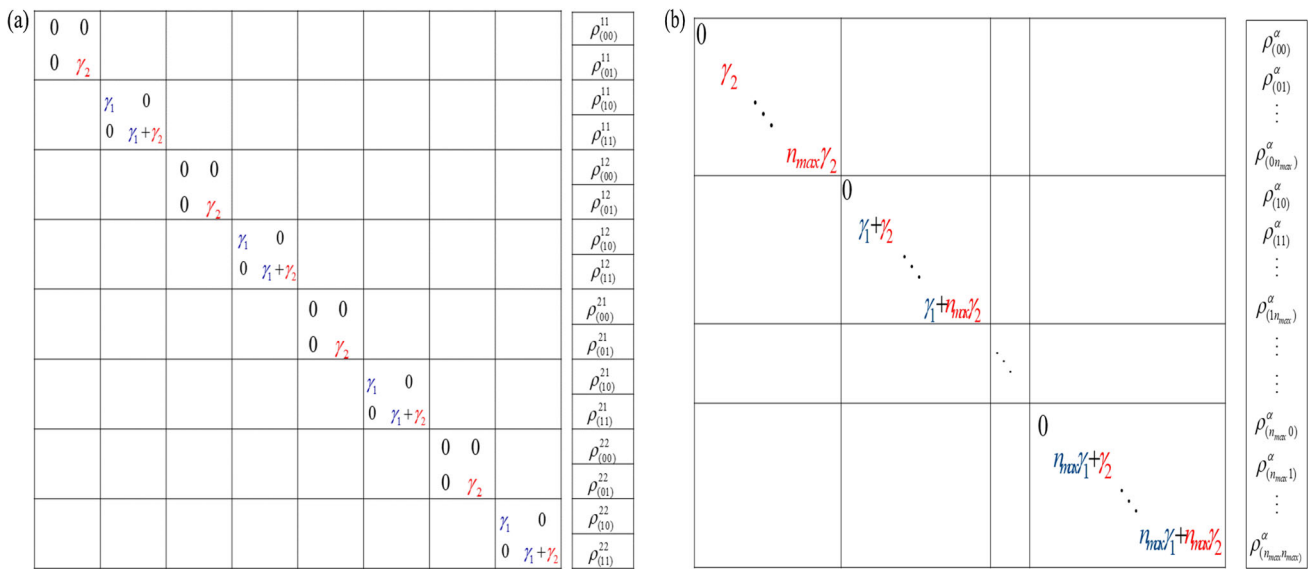


Fig. 5 Color on line. Damping super-operator $(\mathcal{L}_1 + \mathcal{L}_2)/i$ (Eqs. (31) and (32)). **a** Example of a two-state system with two artificial decay modes and $n_{\max} = 1$. \mathcal{L}_1 in blue and \mathcal{L}_2 in red. **b** Block related to a particular element ρ_n^α , where $\alpha = ij$, when $n_{\max} > 1$. All the blocks (ij) have the same structure

The two contributions $\mathcal{L}_{k' +}$ for two decay modes and $n_{\max} > 1$ are:

$$\begin{aligned} \mathcal{L}_{1+} &= -iQ_+ \otimes M' \otimes I_{n_{\text{NHEOM}}} \\ &= -i \begin{pmatrix} 0 & 0 & 0 & 0 \\ 0 & -1 & 0 & 0 \\ 0 & 0 & 1 & 0 \\ 0 & 0 & 0 & 0 \end{pmatrix} \otimes \begin{pmatrix} 0 & 1 & & \\ & 0 & \ddots & \\ & & \ddots & 1 \\ & & & 0 \end{pmatrix} \\ &\quad \otimes \begin{pmatrix} 1 & & & \\ & 1 & & \\ & & \ddots & \\ & & & 1 \end{pmatrix} \end{aligned} \tag{35}$$

and

$$\begin{aligned} \mathcal{L}_{2+} &= -iQ_+ \otimes I_{n_{\text{NHEOM}}} \otimes M' \\ &= -i \begin{pmatrix} 0 & 0 & 0 & 0 \\ 0 & -1 & 0 & 0 \\ 0 & 0 & 1 & 0 \\ 0 & 0 & 0 & 0 \end{pmatrix} \otimes \begin{pmatrix} 1 & & & \\ & 1 & & \\ & & \ddots & \\ & & & 1 \end{pmatrix} \\ &\quad \otimes \begin{pmatrix} 0 & 1 & & \\ & 0 & \ddots & \\ & & \ddots & 1 \\ & & & 0 \end{pmatrix}. \end{aligned} \tag{36}$$

When $n_{\max} = 1$, $I_{n_{\text{NHEOM}}} = I_2$ and $M' = \begin{pmatrix} 0 & 1 \\ 0 & 0 \end{pmatrix}$. The corresponding matrix of the sum $(\mathcal{L}_{1+} + \mathcal{L}_{2+})/(-i)$ is displayed in Fig. 6. By comparing with Eq. (22), the

contribution to $\dot{\rho}_{00}$ of the term related to the upper ADOs with only single excitation is $-i[S, \rho_{10} + \rho_{01}]$, i.e., $\dot{\rho}_{00}^{12} \rightarrow -\rho_{01}^{12} - \rho_{10}^{12}$, $\dot{\rho}_{00}^{21} \rightarrow \rho_{01}^{21} + \rho_{10}^{21}$ and $\dot{\rho}_{00}^{11} = \dot{\rho}_{00}^{22} \rightarrow 0$. Matrix–vector products of lines 5 and 9 with the column vector ρ_n^α in Fig. 6 provide these expressions for the contribution to $\dot{\rho}_{00}^{12}$ and $\dot{\rho}_{00}^{21}$, respectively. The results for $\dot{\rho}_{00}^{11}$ and $\dot{\rho}_{00}^{22}$ can be obtained in the same way at lines 1 and 13.

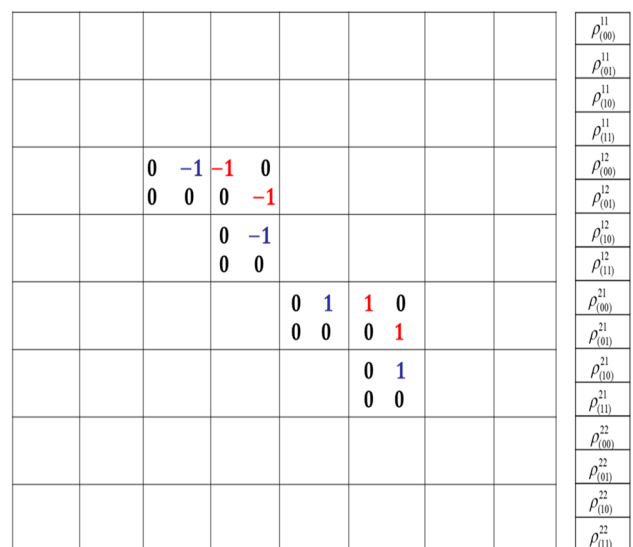


Fig. 6 Matrix $(\mathcal{L}_{1+} + \mathcal{L}_{2+})/(-i)$ in the case of a two-state system with two artificial decay modes and $n_{\max} = 1$. \mathcal{L}_{1+} in blue and \mathcal{L}_{2+} in red

3.2.4 Matrix \mathcal{L}_-

The super-operator connecting the ADOs with a lower layer in the hierarchy involves the operator:

$$\mathcal{L}_{k'-} = -i(\alpha_{k',t/c} S_{k'} \otimes I_n - \tilde{\alpha}_{k',t/c} I_n \otimes S_{k'}) \otimes \prod_{k''=1}^K M''_{k''}, \tag{37}$$

where $M''_{k''} = I_{n_{\text{HEOM}}}$ if $k'' \neq k'$ and $M''_{k'',lm} = (l-1)\delta_{l-1,m}$ if $k'' = k'$ ($l, m \in [1, n_{\text{HEOM}}]$). In the two-level case with $S_{k'}$ independent of k' , for each mode, one has the factor:

$$\begin{aligned} Q_{-k'} &= \alpha_{k'} S \otimes I_n - \tilde{\alpha}_{k'} I_n \otimes S \\ &= \alpha_{k'} \begin{pmatrix} 0 & 0 \\ 0 & 1 \end{pmatrix} \otimes \begin{pmatrix} 1 & 0 \\ 0 & 1 \end{pmatrix} - \tilde{\alpha}_{k'} \begin{pmatrix} 1 & 0 \\ 0 & 1 \end{pmatrix} \otimes \begin{pmatrix} 0 & 0 \\ 0 & 1 \end{pmatrix} \\ &= \begin{pmatrix} 0 & 0 & 0 & 0 \\ 0 & -\tilde{\alpha}_{k'} & 0 & 0 \\ 0 & 0 & \alpha_{k'} & 0 \\ 0 & 0 & 0 & \alpha_{k'} - \tilde{\alpha}_{k'} \end{pmatrix}. \end{aligned} \tag{38}$$

The two contributions to the super-Liouvillian when $n_{\text{max}} > 1$ are:

$$\begin{aligned} \mathcal{L}_{1-} &= Q_{-1} \otimes M'' \otimes I_{n_{\text{HEOM}}} \\ &= \begin{pmatrix} 0 & 0 & 0 & 0 \\ 0 & -\tilde{\alpha}_1 & 0 & 0 \\ 0 & 0 & \alpha_1 & 0 \\ 0 & 0 & 0 & \alpha_1 - \tilde{\alpha}_1 \end{pmatrix} \otimes \begin{pmatrix} 0 \\ 1 \\ 2 \cdots \\ \cdots \cdots \\ n_{\text{max}} 0 \end{pmatrix} \\ &\quad \otimes \begin{pmatrix} 1 \\ 1 \\ \cdots \\ 1 \end{pmatrix} \end{aligned} \tag{39}$$

and

$$\begin{aligned} \mathcal{L}_{2-} &= Q_{-2} \otimes I_{n_{\text{HEOM}}} \otimes M'' \\ &= \begin{pmatrix} 0 & 0 & 0 & 0 \\ 0 & -\tilde{\alpha}_2 & 0 & 0 \\ 0 & 0 & \alpha_2 & 0 \\ 0 & 0 & 0 & \alpha_2 - \tilde{\alpha}_2 \end{pmatrix} \otimes \begin{pmatrix} 1 \\ 1 \\ \cdots \\ 1 \end{pmatrix} \\ &\quad \otimes \begin{pmatrix} 0 \\ 1 \\ 2 \cdots \\ \cdots \cdots \\ n_{\text{max}} 0 \end{pmatrix}. \end{aligned} \tag{40}$$

								$\rho_{(00)}^{11}$
								$\rho_{(01)}^{11}$
								$\rho_{(10)}^{11}$
								$\rho_{(11)}^{11}$
		0 0						$\rho_{(00)}^{12}$
		$-\tilde{\alpha}_2$ 0						$\rho_{(01)}^{12}$
		$-\tilde{\alpha}_1$ 0	0 0					$\rho_{(10)}^{12}$
		0 $-\tilde{\alpha}_1$	$-\tilde{\alpha}_2$ 0					$\rho_{(11)}^{12}$
				0 0				$\rho_{(00)}^{21}$
				$\tilde{\alpha}_2$ 0				$\rho_{(01)}^{21}$
				$\tilde{\alpha}_1$ 0	0 0			$\rho_{(10)}^{21}$
				0 $\tilde{\alpha}_1$	$\tilde{\alpha}_2$ 0			$\rho_{(11)}^{21}$
						0 0		$\rho_{(00)}^{22}$
						$\alpha_2 - \tilde{\alpha}_2$ 0		$\rho_{(01)}^{22}$
						$\alpha_1 - \tilde{\alpha}_1$ 0	0 0	$\rho_{(10)}^{22}$
						0 $\alpha_1 - \tilde{\alpha}_1$	$\alpha_2 - \tilde{\alpha}_2$ 0	$\rho_{(11)}^{22}$

Fig. 7 Matrix $(\mathcal{L}_{1-} + \mathcal{L}_{2-})/(-i)$ in the case of a two-state system with two artificial decay modes and $n_{\text{max}} = 1$. \mathcal{L}_{1+} in blue and \mathcal{L}_{2+} in red

In the example of the two decay modes with $n_{\text{max}} = 1$, one has $M'' = \begin{pmatrix} 0 & 0 \\ 1 & 0 \end{pmatrix}$. The matrices for \mathcal{L}_{1-} and \mathcal{L}_{2-} are given in Fig. 7.

3.3 Dynamics with tensor-train format

Dynamics is driven by solving

$$\dot{\bar{\rho}}(t) = \mathcal{L}\bar{\rho}(t), \tag{41}$$

where $\bar{\rho}$ is the full TT-converted vector of the elements of all the ADOs and \mathcal{L} is the super-operator described in Sect. 3.2. We use the projector-splitting KSL scheme [9, 19, 120, 121] implemented in the ttpy package (tt.ksl.ksl) [122]. The method is based on the dynamical low-rank approximation which is equivalent to the Dirac–Frenkel time-dependent variational principle used in MCTDH. It consists in using an approximate low-rank tensor with fixed ranks instead of getting a solution with a high rank tensor and then truncate it with singular value decomposition (SVD). To comply with this goal, the derivative of the approximate low-rank tensor is obtained by orthogonally projecting the derivative of the tensor on the tangent space of the approximate low-rank tensor at its current position. Time integration is then obtained by a splitting scheme (second order in this work) of the projector (see Refs. [9, 19, 120, 121] for more details). An adaptive rank may be necessary during the propagation as proposed in Refs. [123, 124]. We have adopted a mixed strategy. The standard Runge–Kutta integrator (written with TT algebra available with the ttpy package) is run after some time steps to allow the increase of the ranks during the propagation. In the application, we use a Runge–Kutta run after 10 timesteps.

4 Illustrative applications

We give three examples for which dynamics is driven by the TT method. In the first two cases, the spectral density is continuous and is an Ohmic two-pole Lorentzian function (Eq. (9)) leading to two artificial bath modes. The third application uses undamped discrete modes.

4.1 Population-to-coherence transfer via a bath

The zero-order model and the eigenstates are schematized in Fig. 8. This model was introduced to analyze one of the first applications of an experimental ‘quantum simulator’ for molecular quantum dynamics [125]. As we show, using a circuit of qubits to represent a network of chromophores gives access to strongly non-Markovian regimes of open dynamics, including situations in which strong dissipation actually induces coherent dynamics. Indeed, one of the original motivations for the experiment and analysis of Ref. [126] was to explore the existence, robustness and uses of coherent transport in photosynthetic light-harvesting proteins, which are described by analogous models. However, they are much harder to control compared to superconducting circuits. The Hamiltonian of the active subsystem is:

$$H_S(t) = H_s + H_{\text{ren}} - \sum_{n=0}^3 \sum_{m \neq n=0}^3 \mu_{nm} |n\rangle \langle m| \mathcal{E}(t) \quad (42)$$

with

$$H_s = \sum_{n=0}^3 \varepsilon_n |n\rangle \langle n| + \sum_{n=0}^3 \sum_{m \neq n=0}^3 H_{nm} |n\rangle \langle m|, \quad (43)$$

where H_{ren} is the renormalization term given below and μ_{ij} is the dipolar coupling. The ground state is coupled to the excited states only radiatively, i.e., $H_{0j} = 0$ for

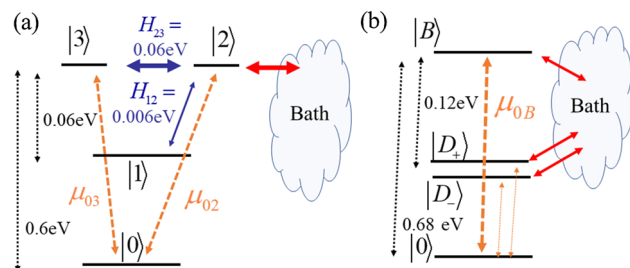


Fig. 8 Schematic representation of the energy levels, the interstate couplings H_{ij} , the dipolar couplings μ_{ij} , and the system–bath couplings of a device in which a long-lasting coherence in a dark doublet may be created by interaction with a bath after excitation of a bright state. **a** zero-order basis, **b** eigenstates

$j \neq 0$ and only μ_{02} and μ_{03} induce the radiative coupling. Two degenerate excited bright states ($|2\rangle$ and $|3\rangle$) strongly interact by interstate coupling H_{23} and state $|2\rangle$ is weakly coupled to a dark lower state $|1\rangle$ and to a tuning bath that makes fluctuate the energy. The strong H_{23} coupling leads to eigenstates that are mainly the bright in phase and the dark out of phase superpositions denoted $|B\rangle$ and $|D_+\rangle$, respectively. Both eigenstates $|D_+\rangle$ and $|D_-\rangle$ form a dark doublet. Their dipole transition moments μ_{0D_\pm} are very weak, being two orders of magnitude smaller than the transition moment μ_{0B} to the $|B\rangle$ state. Spontaneous radiative decay is not taken into account in the simulation.

The bath is coupled to state $|2\rangle$ only. The corresponding system–bath operator takes the form:

$$S = \begin{pmatrix} 0 & 0 & 0 & 0 \\ 0 & 0 & 0 & 0 \\ 0 & 0 & 1 & 0 \\ 0 & 0 & 0 & 0 \end{pmatrix}. \quad (44)$$

The spectral density is highly structured and peaks nearly at the mean ($\Delta_{B-D} = \langle B|H_s|B\rangle - \langle D|H_s|D\rangle$) transition energy, $\langle D|H_s|D\rangle$ being the average energy of states $\langle D_+|H_s|D_+\rangle$ and $\langle D_-|H_s|D_-\rangle$. It is a single Ohmic Lorentzian (Eq. (9)) with parameters $p = 2.0 \times 10^{-12}$ a.u., $\Omega = 4.5 \times 10^{-3}$ a.u. and $\Gamma = 4.0 \times 10^{-4}$ a.u. It is represented with the correlation function at $T = 298$ K in Fig. 9. The renormalization energy is $\lambda = (1/\pi) \int_0^\infty d\omega J(\omega)/\omega$. The corresponding renormalization term is $H_{\text{ren}} = \lambda|2\rangle\langle 2|$. The system–bath coupling is weak. It is estimated by the ratio $\eta = \lambda/\Delta_{(|B\rangle-|D\rangle)}$ where $\Delta_{(|B\rangle-|D\rangle)}$ is the energy gap

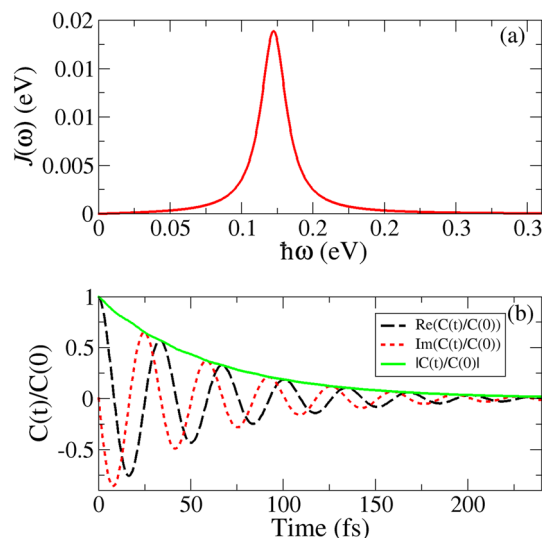


Fig. 9 **a** Spectral density of the model presented in Fig. 8 to illustrate the population-to-coherence transfer. The spectral density maximum is close to the mean BD energy gap; **b** corresponding normalized correlation function $C(t)/C(0)$ (Eq. (4)) at $T = 298$ K with real part (dashed line), imaginary part (dots) and modulus (solid line)

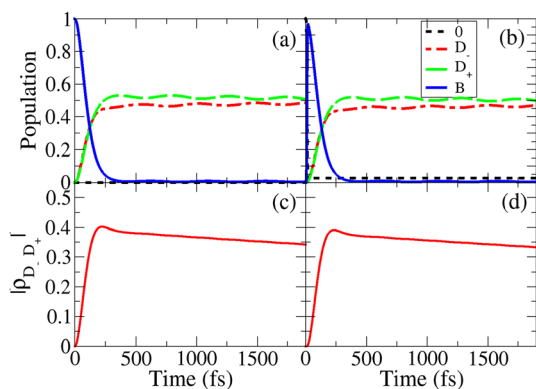


Fig. 10 Upper panels: populations in the eigenstates B , D_- and D_+ , **a** ideal preparation in the bright state B , **b** excitation of the B state from the ground state by a π pulse of 24 fs. Lower panels: modulus of the coherence $(\rho_S)_{D_+D_-}$, **c** ideal preparation in the bright state, **d** excitation by a π pulse

corresponding here to the cutoff of the spectral density. It is a perturbative regime; however, the correlation time is long (about 250 fs) due to the peaked shape of the spectral density. It is longer than the Rabi period of the $(|B\rangle - |D\rangle)$ transition that is 34 fs. Dynamics is then non-Markovian with $n_{\text{HEOM}} = 5$.

In the eigenstate representation (Fig. 8b), the S operator becomes:

$$S_{\text{eigen}} = \begin{pmatrix} 0 & 0 & 0 & 0 \\ 0 & 0.26 & 0.25 & 0.36 \\ 0 & 0.25 & 0.24 & 0.34 \\ 0 & 0.36 & 0.34 & 0.50 \end{pmatrix}. \quad (45)$$

In this basis set, the bath is coupled diagonally and off-diagonally to the system. This is an interesting device leading to a population-to-coherence transfer from the bright $|B\rangle$ state to the dark doublet. This process requires exact non-Markovian dynamics taking terms that are neglected in the secular approximation of a Redfield treatment [126, 127]. From the analysis in Ref. [126], we choose a coupling strength $\eta = 0.013$ relevant to illustrate an efficient population-to-coherence process. The populations in the eigenstates and the modulus of the coherence $(\rho_S)_{D_+D_-}$ between the two dark states are displayed in Fig. 10a and c when the initial state is the bright state $|B\rangle$. In this ideal case, the population-to-coherence is complete in 250 fs. The coherence is long-lasting and slowly decays in about 25 ps. Figure 10b and d compare this ideal preparation with the results obtained by an excitation from the ground state by a laser field of 24 fs. To respect the condition that the area of the oscillating field must be equal to zero [128, 129], the field is then given by $\mathcal{E}(t) = -\frac{\partial A(t)}{\partial t}$ with the vector potential $\mathcal{A}(t) = \left(\frac{\mathcal{E}_0}{\omega}\right) \sin^2\left(\frac{\pi(t-t_i)}{\tau}\right) \sin(\omega(t-t_i))$, where t_i is the initial time of the pulse, $t_i = 0$ here, τ is the pulse duration and \mathcal{E}_0 is the field maximum amplitude. The

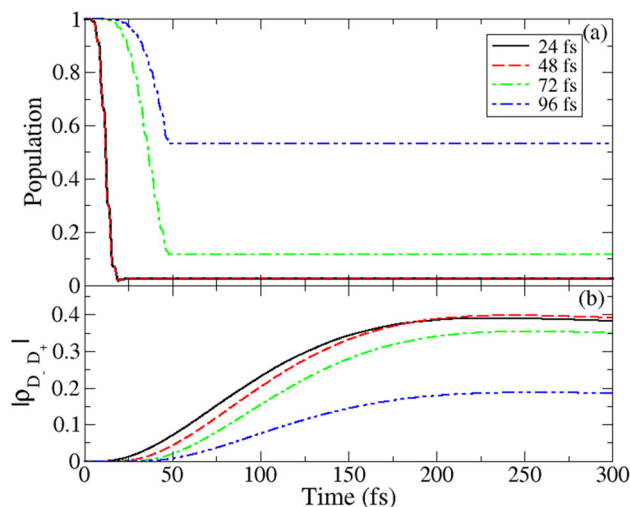


Fig. 11 Excitation of the bright state B by a π pulse of different durations. **a** Population in the ground state, **b** modulus of the coherence $(\rho_S)_{D_+D_-}$ generated in the dark doublet

carrier frequency is in resonance with the $|0\rangle \rightarrow |B\rangle$ transition. When the number of cycles is large for a pulse duration longer than about 20 fs, the expression becomes similar to a pulse with a sine square envelope $\mathcal{E}(t) = \mathcal{E}_0 \sin^2\left(\frac{\pi t}{\tau}\right) \cos(\omega_0 B t)$. We use this expression to estimate \mathcal{E}_0 providing a π pulse for which the integral of the Rabi frequency $\Omega(t) = \mathcal{E}_0 \sin^2\left(\frac{\pi t}{\tau}\right) \mu_{0B} / \hbar$ is equal to π [130, 131]. μ_{0B} is the transition dipole. Then, $\mathcal{E}_0 = 2\pi / (\mu_{0B} \tau)$. This field would induce a complete transfer towards the bright state in the absence of coupling to the bath. A slight modification of the amplitude should be necessary for short pulses with few cycles for which the envelope slightly differs from a sine square.

Figure 11 shows the influence of the pulse duration τ on the coherence generation in the dark doublet. The result is close to the ideal case for pulses with τ in the range 20–50 fs. The decrease of the yield comes from the environment that makes fluctuate the energies.

Simulations are made with a timestep of 0.24 fs and the maximum rank is 10 with $\epsilon = 10^{-15}$. The temperature is 298 K. No Matsubara term is needed due to the high temperature and the narrow spectral density. No significant change has been observed when carrying out this simulation with 3 additional Matsubara terms.

4.2 Simulation of absorption and emission spectra

HEOM have already been used to simulate stationary absorption σ_{abs} and emission σ_{em} spectra [23, 24, 132–135]. They are computed by the linear response theory as:

$$\sigma_{abs}(\omega) = \text{Re} \int_0^\infty dt e^{i\omega t} \text{Tr}_S \left[\rho_{\mu^-}^\dagger(t) \rho_{\mu^-}(0) \right], \quad (46)$$

$$\sigma_{em}(\omega) = \text{Re} \int_0^\infty dt e^{i\omega t} \text{Tr}_S \left[\rho_{\mu^+}^\dagger(t) \rho_{\mu^+}(t_{\text{eq}}) \right], \quad (47)$$

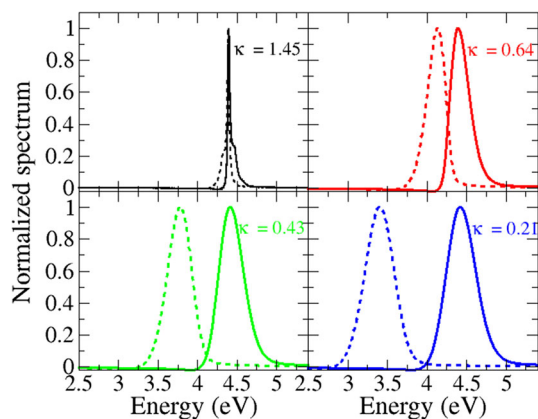


Fig. 14 Normalized absorption (solid lines) and emission (dashed lines) spectra for the case with a single bright state ($H_{12} = 0$) represented in Fig. 12. The panels correspond to the different spectral densities given in Fig. 13. κ is defined in Eq. (49)

eV. In this example, the relaxation is simply the evolution towards the thermal mixture at the new equilibrium geometry of the excited bright state. This stationary state is obtained in about 150 fs. The ADOs are taken after a propagation of 180 fs. Generally, the computation of the emission spectrum is more demanding than for the absorption. Convergence of the correlation function requires higher HEOM level (up to level 55 for $\kappa = 0.21$). Propagation with the TT method has required a small time step of 0.012 fs. The maximum tensor rank remains below 10 with $\epsilon = 10^{-20}$. The spectra are computed at 298 K. We have verified for the case with $\kappa = 0.21$ that no Matsubara term is necessary.

(ii) In the second example presented in Fig. 15, dynamics is more complicated since the emission occurs from the eigen vibronic states having a component on the bright state. The propagation duration to reach the asymptotic populations and prepare the ADOs depends on λ . It is 500 or 600 fs for the different examples. The absorption spectrum is more affected by the nonadiabatic interaction. For the emission spectrum, one recovers the shape corresponding to the relaxed bright state in this example since the second excited state is assumed to be dark. The evolution of the Stokes shift with respect to the κ parameter is the same and corresponds to the expected behavior.

These results highlight that tools like HEOM can now predict optical spectra with great precision, given the spectral density. Therefore, attention must now be given to extracting high-quality spectral densities to match experimental results, particularly in condensed phases where there can be very distinct timescales in the environment, i.e., fast intramolecular motions and slow solvent/lattice/protein reorganization. The importance of including the latter and a way of obtaining them from first principles was given in Ref. [15].

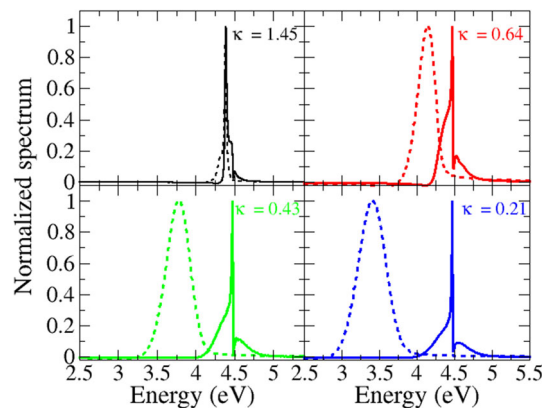


Fig. 15 Normalized absorption (solid lines) and emission (dashed lines) spectra for the case with a bright state coupled to a dark state ($H_{12} \neq 0$) represented in Fig. 12. The panels correspond to the different spectral densities given in Fig. 13. κ is defined in Eq. (49)

4.3 Excitation transfer with discrete bath modes

In this example, the bath is formed by discrete undamped vibrational modes. We revisit the excitation transfer in a dimer oligothiophene (OT₄)-fullerene(C₆₀) investigated by I. Burghardt and coworkers [67, 93, 95, 136]. The excited states may be schematized as in Fig. 12 with D being the excitonic state XT and B becoming the charge transfer (CT) state. We consider the parameters for an inter-fragment distance of 0.35 nm [67]. The energy gap is 0.07 eV and the electronic coupling is 0.007 eV. The continuous spectral density has been obtained from the difference of the equilibrium position Δq_{eq} of the fragment normal modes [136]. The reference position of the equilibrated bath is taken at the middle point $\Delta q_{\text{eq}}/2$ so that the coupling operator is

$$S = \begin{pmatrix} -0.5 & 0 \\ 0 & 0.5 \end{pmatrix}. \quad (50)$$

The smooth spectral density [93] is fitted by five two-pole Lorentzians (Eq. (9)) and displayed in Fig. 16a. The parameters are given in the supplementary material of Ref. [67]. This leads to $K = 10$ artificial decay modes without Matsubara terms at 298 K. We have used the discretization procedure of Ref. [137] providing unequally spaced modes that correspond to equal fractions of the reorganization energy. The discrete spectral density at the $N_{\text{disc}} = 40$ selected points k ($\pi c_k^2 / (2\omega_k \Delta(\omega))$, where $\Delta(\omega)$ is the local state density) is shown in Fig. 16b. Since two baths are involved in the discrete procedure, this corresponds to $K = 80$ modes. Figure 16c gives the occupation probability of the XT and CT states when the initial state is XT. The dashed lines are obtained with the continuous spectral density and the five artificial modes, at level 5 of the hierarchy, with the tolerance parameter $\epsilon = 10^{-10}$ and the maximum rank (rmax) is 20 (see Appendix).

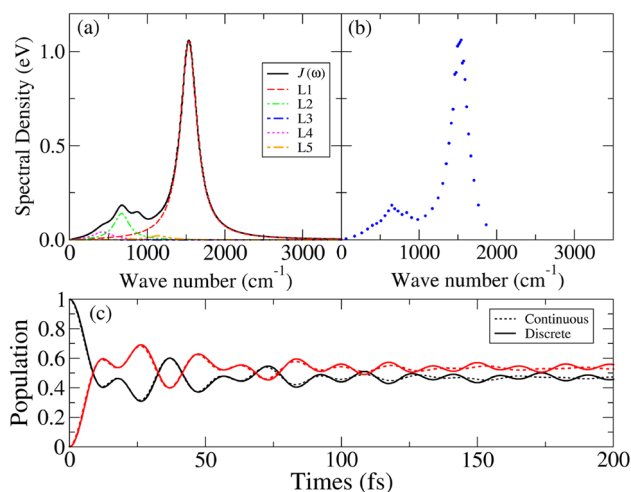


Fig. 16 Excitation energy transfer dynamics with a continuous or discretized spectral density by the TT implementation. **a** Continuous spectral density fitted by five two-pole Lorentzian functions (Eq. (9)), see Refs. [67, 93], **b** discretization in $N_{\text{disc}} = 40$ modes by the Makri procedure (see Ref. [137]) leading to $K = 2N_{\text{disc}}$ decay modes, **c** population in the XT (black) and CT (red) states when the initial state is XT. Dashed lines: TT implementation with the continuous spectral density leading to $K = 10$ decay modes without Matsubara terms at 298 K; solid lines: TT implementation with $K = 80$ discrete modes

This example requires only 3003 matrices and the TT formulation is not more advantageous than the standard one. However, the discrete case may emphasize the utility of the TT propagation when compared with a standard treatment. The corresponding population are drawn in solid lines in Fig. 16c. We may estimate the total number of elements in the full matrix array. One has $n = 2$, $K = 80$, $L = 5$ leading to $N_{\text{standard}} = n^2(K + L)! / (K!L!) = 131,206,068$ elements. This is a computationally heavy simulation (≈ 21 GB for the density matrix only) and intractable with our current Fortran implementation. In the TT implementation, one has $n = 2$, $K = 80$, $L = 5$ and $r_{\text{max}} = 80$. The number of stored elements might reach a maximum value of $N_{TT} = (n^2 + L) * r_{\text{max}} + r_{\text{max}}^2 * (K - 1) * L = 2,528,720$. The storage is obviously more attractive (≈ 400 MB). The tolerance is $\epsilon = 10^{-8}$. The norm is well conserved up to about 250 fs. The result is promising but it will be necessary to improve the adaptation of the maximum rank to further extend the performance [33, 123].

5 Conclusion

We have given a detailed description of the TT formulation of HEOM and how it is implemented which we hope will be a useful guide to newcomers to the field. This is an exciting development, linking the widely used HEOM method with rapidly developing advances in

tensor networks across physics and theoretical chemistry. One could connect to them the recent explosion of physical science applications of machine learning, for example: tensor network simulation of multi-environmental open quantum dynamics via machine learning [138, 139] and entanglement renormalization [140].

We have shown three examples where the TT method allows us to obtain highly accurate results for complex phenomena, such as ‘noisy’ generation of coherences (population to coherence transfer) and the dramatic impact of bath relaxation times on optical spectra. The latter is important, as Stokes shifts are often used as a direct measure of system–bath coupling. This is clearly only one part of the story, as the relaxation time is also important. Hence, suitable techniques that can handle multiple timescales (long and short-lived ADOs) are essential. These effects described above will be even more important in larger multistate systems. The third example simulates an ultrafast excitation transfer using only undamped decay modes. This example illustrates the efficiency of the TT formulation when compared to the standard method, which would involve a huge number of matrices. All the applications involve non-Markovian dynamics, either due to long correlation times or high level of hierarchy.

It would be interesting to consider extensions to time-dependent spectroscopies, 2D spectroscopies [24, 56–58], and optical control. Adaptation of the TT formulation for optimal control has already been given in Ref. [50]. Another important prospect is the consideration of non-harmonic environments, for instance by including some modes in the active system [43, 45, 67, 68] and the treatment of fermionic baths [55, 81].

Acknowledgements This work was performed within the French GDR 686 3575 THEMES. We want to dedicate this work to the memory of Christoph Meier and Osman Atabek. Both authors made significant contributions to the research areas described above, such as the Meier–Tannor spectral density and the introduction of the auxiliary matrices. Both have also greatly contributed to many strategies of quantum control in a wide range of processes such as molecular orientation, dynamics of excited states, isomerization, molecular cooling to cite only few. Dominik Domin is warmly acknowledged for his efficient technical support.

Author contribution statement

All the authors were involved in the preparation of the manuscript. All the authors have read and approved the final manuscript.

Funding No funding was received for conducting this study.

Availability of data and materials This manuscript has no associated data or the data will not be deposited. [Authors’ comment: The datasets generated during and/or analyzed during the current study are available from the corresponding author on reasonable request.]

Declarations

Conflict of interest The authors have no relevant financial or non-financial interests to disclose.

Ethics approval Not applicable.

Appendix: Numerical implementation of HEOM with ttpy

Most of the TT algebra is carried out by the ttpy package developed by Oseledets and coworkers [122]. In this appendix, we show a minimal code to build the system Liouvillian and time-integrate a given system density matrix with initial system–bath factorization in TT format with Python3, Numpy and ttpy packages.

The system Liouvillian is defined as $\mathcal{L}_{S(\text{ADO})} = -i(H \otimes I_n - I_n \otimes H)$ where H is the system Hamiltonian, I_n the identity matrix with n the number of system states. Thus, $\mathcal{L}_{S(\text{ADO})}$ is a $n^2 \times n^2$ matrix which can be built from standard numpy functions (`np.eye` returns the identity matrix and `np.kron` the Kronecker product of both matrices):

```
ids = np.eye(n)
Ls = -j * (np.kron(hamil,ids) \
- np.kron(ids,hamil))
```

where `ids` is the identity matrix of size $n \times n$ and j the imaginary unit. To convert this numpy array to a TT format, `tt.matrix` routine performs an approximation of $\mathcal{L}_{S(\text{ADO})}$ for a maximal rank (`rmax`) and an accuracy `eps`:

```
Ls = tt.matrix(Ls, eps=eps, rmax=rmax)
```

where `Ls` is the system Liouvillian super-operator. At this point, we are still only dealing with a representation of an array of $n^2 \times n^2$ dimensions. The HEOM super-operator \mathcal{L}_S which spans over the whole Liouville space is defined as $\mathcal{L}_S = \mathcal{L}_{S(\text{ADO})} \otimes \prod_{k''=1}^K I_{n_{\text{HEOM}}}$. To avoid memory issues due to the high dimensionality of the array, one must work with the Kronecker products (`tt.kron`) of ttpy packages instead of the one of numpy (`np.kron`). Indeed, numpy will build the full tensor which can be very large and thus might suffer from the dimensionality curse. To carry out this task, a single loop iterates over the number of artificial decay modes K with successive Kronecker products:

```
idr = np.eye(nheom)
idr = tt.matrix(idr)
for i in range(K):
    Ls = tt.kron(Ls,idr)
```

The total Liouvillian super-operator \mathcal{L} is a sum of several other super-operators, i.e., $\mathcal{L}_{k'}$, $\mathcal{L}_{k'+}$, $\mathcal{L}_{k'-}$

(see Eq. (26)). Addition can be performed directly with the usual algebraic symbol (+) on TT objects. The ttpy library carries out automatically the correct tensor operations. However, tensor ranks increase at each iteration. Thus, rounding operations are regularly performed to reduce the rank for a given accuracy and maximum rank with the following command:

```
L = L.round(eps,rmax)
```

where `L` is the total HEOM Liouvillian super-operator.

The initial vectorized density matrix is defined directly from its cores. The first core is filled with the initial system density matrix. As all auxiliary density matrices are vectors of zeros when assuming system–bath factorization all the other cores are vectors of dimensions n_{HEOM} with only the first index equal to 1.

For a given system density matrix `rho` defined as a numpy array and `r` the initial core rank (equal to 1) in this example, we compute `rho` the initial density matrix in TT format with the following algorithm:

```
rho = np.zeros((n**2), \
dtype=np.complex128)
rho = np.reshape(rhos,n**2)
cores = []
a = np.zeros((1,n**2,r))
a[0,:,0] = rho.copy()
cores.append(a)
vec = np.zeros((nheom), \
dtype=np.complex128)
vec[0] = 1.
for i in range(K-1):
    a = np.zeros((r,nheom,r))
    a[0,:,0] = vec[:]
    cores.append(a)
a = np.zeros((r,nheom,1))
a[0,:,0] = vec[:]
cores.append(a)
rho = tt.vector().from_list(cores)}
```

Time integration is performed with the KSL second-order splitting algorithm [120]. For each time step `dt`, the density matrix in TT format is updated using the function `ksl` implemented in `tt.ksl` routines:

```
rho = tt.ksl.ksl(L,rho,dt)
```

By iterating over the desired number of timesteps, we compute the full density matrix at time t . To extract the system density matrix, projection techniques (by expressing projectors on the full Liouville space in the TT format) or core manipulations can be used.

References

1. U. Manthe, A multilayer multiconfigurational time-dependent Hartree approach for quantum dynamics

- on general potential energy surfaces. *J. Chem. Phys.* **128**(16), 164116 (2008). <https://doi.org/10.1063/1.2902982>
2. H. Wang, M. Thoss, Numerically exact quantum dynamics for indistinguishable particles: the multilayer multiconfiguration time-dependent Hartree theory in second quantization representation. *J. Chem. Phys.* **131**(2), 024114 (2009). <https://doi.org/10.1063/1.3173823>
 3. O. Vendrell, H.D. Meyer, Multilayer multiconfiguration time-dependent Hartree method: implementation and applications to a Henon–Heiles Hamiltonian and to pyrazine. *J. Chem. Phys.* **134**(4), 044135 (2011). <https://doi.org/10.1063/1.3535541>
 4. L.P. Lindoy, B. Kloss, D.R. Reichman, Time evolution of ML-MCTDH wavefunctions. II. Application of the projector splitting integrator. *J. Chem. Phys.* **155**(17), 174109 (2021). <https://doi.org/10.1063/5.0070043>
 5. T.G. Kolda, B.W. Bader, Tensor decompositions and applications. *SIAM Rev.* **51**(3), 455–500 (2009). <https://doi.org/10.1137/07070111X>
 6. L. Grasedyck, D. Kressner, C. Tobler, A literature survey of low-rank tensor approximation techniques. *GAMM-Mitteilungen* **36**(1), 53–78 (2013). <https://doi.org/10.1002/gamm.201310004>
 7. I.V. Oseledets, Tensor-train decomposition. *SIAM J. Sci. Comput.* **33**(5), 2295–2317 (2011). <https://doi.org/10.1137/090752286>
 8. C. Lubich, I.V. Oseledets, B. Vandereycken, Time integration of tensor trains. *SIAM J. Numer. Anal.* **53**(2), 917–941 (2015). <https://doi.org/10.1137/140976546>
 9. J. Haegeman, C. Lubich, I. Oseledets, B. Vandereycken, F. Verstraete, Unifying time evolution and optimization with matrix product states. *Phys. Rev. B* **94**, 165116 (2016). <https://doi.org/10.1103/PhysRevB.94.165116>
 10. R. Orús, A practical introduction to tensor networks: matrix product states and projected entangled pair states. *Ann. Phys.* **349**, 117–158 (2014). <https://doi.org/10.1016/j.aop.2014.06.013>
 11. F.A.Y.N. Schröder, A.W. Chin, Simulating open quantum dynamics with time-dependent variational matrix product states: towards microscopic correlation of environment dynamics and reduced system evolution. *Phys. Rev. B* **93**, 075105 (2016). <https://doi.org/10.1103/PhysRevB.93.075105>
 12. F.A.Y.N. Schröder, D.H.P. Turban, A.J. Musser, N.D.M. Hine, A.W. Chin, Tensor network simulation of multi-environmental open quantum dynamics via machine learning and entanglement renormalisation. *Nat. Commun.* **10**, 1062 (2019)
 13. A.M. Alvertis, F.A.Y.N. Schröder, A.W. Chin, Non-equilibrium relaxation of hot states in organic semiconductors: impact of mode-selective excitation on charge transfer. *J. Chem. Phys.* **151**(8), 084104 (2019)
 14. T. Lacroix, A. Dunnett, D. Gribben, B.W. Lovett, A. Chin, Unveiling non-Markovian spacetime signaling in open quantum systems with long-range tensor network dynamics. *Phys. Rev. A* **104**, 052204 (2021). <https://doi.org/10.1103/PhysRevA.104.052204>
 15. A.J. Dunnett, D. Gowland, C.M. Isborn, A.W. Chin, T.J. Zuehlsdorff, Influence of non-adiabatic effects on linear absorption spectra in the condensed phase: methylene blue. *J. Chem. Phys.* **155**(14), 144112 (2021). <https://doi.org/10.1063/5.0062950>
 16. A. Baiardi, M. Reiher, Large-scale quantum dynamics with matrix product states. *J. Chem. Theory Comput.* **15**(6), 3481–3498 (2019). <https://doi.org/10.1021/acs.jctc.9b00301>
 17. X. Xie, Y. Liu, Y. Yao, U. Schollwöck, C. Liu, H. Ma, Time-dependent density matrix renormalization group quantum dynamics for realistic chemical systems. *J. Chem. Phys.* **151**(22), 224101 (2019). <https://doi.org/10.1063/1.5125945>
 18. A.D. Somoza, O. Marty, J. Lim, S.F. Huelga, M.B. Plenio, Dissipation-assisted matrix product factorization. *Phys. Rev. Lett.* **123**, 100502 (2019). <https://doi.org/10.1103/PhysRevLett.123.100502>
 19. N. Lyu, M.B. Soley, V.S. Batista, Tensor-train split-operator KSL (TT-SOKSL) method for quantum dynamics simulations. *J. Chem. Theory Comput.* **18**(6), 3327–3346 (2022). <https://doi.org/10.1021/acs.jctc.2c00209>
 20. P. Gelß, R. Klein, S. Matera, B. Schmidt, Solving the time-independent Schrödinger equation for chains of coupled excitons and phonons using tensor trains. *J. Chem. Phys.* **156**(2), 024109 (2022). <https://doi.org/10.1063/5.0074948>
 21. R. Feynman, F. Vernon, The theory of a general quantum system interacting with a linear dissipative system. *Ann. Phys.* **24**, 118–173 (1963). [https://doi.org/10.1016/0003-4916\(63\)90068-X](https://doi.org/10.1016/0003-4916(63)90068-X)
 22. Y. Tanimura, R. Kubo, Time evolution of a quantum system in contact with a nearly Gaussian–Markoffian noise bath. *J. Phys. Soc. Jpn.* **58**(1), 101–114 (1989). <https://doi.org/10.1143/JPSJ.58.101>
 23. Y. Tanimura, Stochastic Liouville, Langevin, Fokker–Planck, and master equation approaches to quantum dissipative systems. *J. Phys. Soc. Jpn.* **75**(8), 082001 (2006). <https://doi.org/10.1143/JPSJ.75.082001>
 24. Y. Tanimura, Numerically “exact” approach to open quantum dynamics: the hierarchical equations of motion (HEOM). *J. Chem. Phys.* **153**(2), 020901 (2020). <https://doi.org/10.1063/5.0011599>
 25. R.X. Xu, Y. Yan, Dynamics of quantum dissipation systems interacting with bosonic canonical bath: hierarchical equations of motion approach. *Phys. Rev. E* **75**, 031107 (2007)
 26. Q. Shi, L. Chen, G. Nan, R.X. Xu, Y. Yan, Efficient hierarchical Liouville space propagator to quantum dissipative dynamics. *J. Chem. Phys.* **130**(8), 084105 (2009). <https://doi.org/10.1063/1.3077918>
 27. S. Nakajima, On quantum theory of transport phenomena: steady diffusion. *Prog. Theor. Phys.* **20**(6), 948–959 (1958). <https://doi.org/10.1143/PTP.20.948>
 28. R. Zwanzig, Ensemble method in the theory of irreversibility. *J. Chem. Phys.* **33**(5), 1338–1341 (1960). <https://doi.org/10.1063/1.1731409>
 29. A. Ishizaki, G.R. Fleming, Unified treatment of quantum coherent and incoherent hopping dynamics in electronic energy transfer: reduced hierarchy equation approach. *J. Chem. Phys.* **130**(23), 234111 (2009). <https://doi.org/10.1063/1.3155372>

30. A. Bose, P.L. Walters, A multisite decomposition of the tensor network path integrals. *J. Chem. Phys.* **156**(2), 024101 (2022). <https://doi.org/10.1063/5.0073234>
31. Q. Shi, Y. Xu, Y. Yan, M. Xu, Efficient propagation of the hierarchical equations of motion using the matrix product state method. *J. Chem. Phys.* **148**(17), 174102 (2018). <https://doi.org/10.1063/1.5026753>
32. Y. Yan, T. Xing, Q. Shi, A new method to improve the numerical stability of the hierarchical equations of motion for discrete harmonic oscillator modes. *J. Chem. Phys.* **153**(20), 204109 (2020). <https://doi.org/10.1063/5.0027962>
33. R. Borrelli, S. Dolgov, Expanding the range of hierarchical equations of motion by tensor-train implementation. *J. Phys. Chem. B* **125**(20), 5397–5407 (2021). <https://doi.org/10.1021/acs.jpcc.1c02724>
34. R. Borrelli, M.F. Gelin, Finite temperature quantum dynamics of complex systems: integrating thermo-field theories and tensor-train methods. *WIREs Comput. Mol. Sci.* **11**(6), e1539 (2021). <https://doi.org/10.1002/wcms.1539>
35. Y. Yan, M. Xu, T. Li, Q. Shi, Efficient propagation of the hierarchical equations of motion using the tucker and hierarchical tucker tensors. *J. Chem. Phys.* **154**(19), 194104 (2021). <https://doi.org/10.1063/5.0050720>
36. A. Ishizaki, T.R. Calhoun, G.S. Schlau-Cohen, G.R. Fleming, Quantum coherence and its interplay with protein environments in photosynthetic electronic energy transfer. *Phys. Chem. Chem. Phys.* **12**, 7319–7337 (2010). <https://doi.org/10.1039/C003389H>
37. C. Kreisbeck, T. Kramer, Long-lived electronic coherence in dissipative exciton dynamics of light-harvesting complexes. *J. Phys. Chem. Lett.* **3**(19), 2828–2833 (2012). <https://doi.org/10.1021/jz3012029>. [arXiv:1203.1485](https://arxiv.org/abs/1203.1485)
38. S. Saito, M. Higashi, G.R. Fleming, Site-dependent fluctuations optimize electronic energy transfer in the Fenna–Matthews–Olson protein. *J. Phys. Chem. B* **123**(46), 9762–9772 (2019). <https://doi.org/10.1021/acs.jpcc.9b07456>. (PMID: 31657928)
39. L. Chen, P. Shenai, F. Zheng, A. Somoza, Y. Zhao, Optimal energy transfer in light-harvesting systems. *Molecules* **20**(8), 15224–15272 (2015). <https://doi.org/10.3390/molecules200815224>. <https://www.mdpi.com/1420-3049/20/8/15224>
40. T.P. Fay, D.T. Limmer, Coupled charge and energy transfer dynamics in light harvesting complexes from a hybrid hierarchical equations of motion approach. *J. Chem. Phys.* **157**(17), 174104 (2022). <https://doi.org/10.1063/5.0117659>
41. M. Cainelli, Y. Tanimura, Exciton transfer in organic photovoltaic cells: a role of local and nonlocal electron–phonon interactions in a donor domain. *J. Chem. Phys.* **154**(3), 034107 (2021). <https://doi.org/10.1063/5.0036590>
42. M. Tanaka, Y. Tanimura, Multistate electron transfer dynamics in the condensed phase: exact calculations from the reduced hierarchy equations of motion approach. *J. Chem. Phys.* **132**(21), 214502 (2010). <https://doi.org/10.1063/1.3428674>
43. E. Mangaud, A. de la Lande, C. Meier, M. Desouter-Lecomte, Electron transfer within a reaction path model calibrated by constrained DFT calculations: application to mixed-valence organic compounds. *Phys. Chem. Chem. Phys.* **17**, 30889–30903 (2015). <https://doi.org/10.1039/C5CP01194A>
44. T. Firmino, E. Mangaud, F. Cailliez, A. Devolder, D. Mendive-Tapia, F. Gatti, C. Meier, M. Desouter-Lecomte, A. de la Lande, Quantum effects in ultrafast electron transfers within cryptochromes. *Phys. Chem. Chem. Phys.* **18**, 21442–21457 (2016). <https://doi.org/10.1039/C6CP02809H>
45. L. Chen, M.F. Gelin, V.Y. Chernyak, W. Domcke, Y. Zhao, Dissipative dynamics at conical intersections: simulations with the hierarchy equations of motion method. *Faraday Discuss.* **194**, 61–80 (2016). <https://doi.org/10.1039/C6FD00088F>
46. H.G. Duan, V.I. Prokhorenko, R.J. Cogdell, K. Ashraf, A.L. Stevens, M. Thorwart, R.D. Miller, Nature does not rely on long-lived electronic quantum coherence for photosynthetic energy transfer. *Proc. Natl. Acad. Sci.* **114**(32), 8493–8498 (2017)
47. A.G. Dijkstra, V.I. Prokhorenko, Simulation of photo-excited adenine in water with a hierarchy of equations of motion approach. *J. Chem. Phys.* **147**(6), 064102 (2017). <https://doi.org/10.1063/1.4997433>
48. E. Mangaud, B. Lasorne, O. Atabek, M. Desouter-Lecomte, Statistical distributions of the tuning and coupling collective modes at a conical intersection using the hierarchical equations of motion. *J. Chem. Phys.* **151**(24), 244102 (2019). <https://doi.org/10.1063/1.5128852>
49. G. Breuil, E. Mangaud, B. Lasorne, O. Atabek, M. Desouter-Lecomte, Funneling dynamics in a phenylacetylene trimer: coherent excitation of donor excitonic states and their superposition. *J. Chem. Phys.* **155**(3), 034303 (2021). <https://doi.org/10.1063/5.0056351>
50. A. Jaouadi, J. Galiana, E. Mangaud, B. Lasorne, O. Atabek, M. Desouter-Lecomte, Laser-controlled electronic symmetry breaking in a phenylene ethynylene dimer: simulation by the hierarchical equations of motion and optimal control. *Phys. Rev. A* **106**, 043121 (2022). <https://doi.org/10.1103/PhysRevA.106.043121>
51. J. Zhang, R. Borrelli, Y. Tanimura, Proton tunneling in a two-dimensional potential energy surface with a non-linear system-bath interaction: Thermal suppression of reaction rate. *The Journal of Chemical Physics* **152**(21), 214–114 (2020). <https://doi.org/10.1063/5.0010580>
52. E. Mangaud, R. Puthumpally-Joseph, D. Sugny, C. Meier, O. Atabek, M. Desouter-Lecomte, Non-Markovianity in the optimal control of an open quantum system described by hierarchical equations of motion. *New J. Phys.* **20**, 043050 (2018)
53. A. Kato, Y. Tanimura, Quantum heat current under non-perturbative and non-Markovian conditions: applications to heat machines. *J. Chem. Phys.* **145**(22), 224105 (2016). <https://doi.org/10.1063/1.4971370>
54. L. Song, Q. Shi, Hierarchical equations of motion method applied to nonequilibrium heat transport in model molecular junctions: transient heat current and high-order moments of the current operator. *Phys. Rev.*

- B **95**(6), 064308 (2017). <https://doi.org/10.1103/PhysRevB.95.064308>
55. J. Bätge, Y. Ke, C. Kaspar, M. Thoss, Nonequilibrium open quantum systems with multiple bosonic and fermionic environments: a hierarchical equations of motion approach. *Phys. Rev. B* **103**, 235413 (2021). <https://doi.org/10.1103/PhysRevB.103.235413>
 56. E.C. Wu, Q. Ge, E.A. Arsenaault, N.H.C. Lewis, N.L. Gruenke, M.J. Head-Gordon, G.R. Fleming, Two-dimensional electronic-vibrational spectroscopic study of conical intersection dynamics: an experimental and electronic structure study. *Phys. Chem. Chem. Phys.* **21**(26), 14153–14163 (2019). <https://doi.org/10.1039/C8CP05264F>
 57. K.B. Zhu, R.X. Xu, H.Y. Zhang, J. Hu, Y.J. Yan, Hierarchical dynamics of correlated system-environment coherence and optical spectroscopy. *J. Phys. Chem. B* **115**(18), 5678–5684 (2011). <https://doi.org/10.1021/jp2002244>
 58. Y. Tanimura, Reduced hierarchy equations of motion approach with Drude plus Brownian spectral distribution: probing electron transfer processes by means of two-dimensional correlation spectroscopy. *J. Chem. Phys.* **137**(22), 22A550 (2012). <https://doi.org/10.1063/1.4766931>
 59. H. Liu, L. Zhu, S. Bai, Q. Shi, Reduced quantum dynamics with arbitrary bath spectral densities: hierarchical equations of motion based on several different bath decomposition schemes. *J. Chem. Phys.* **140**(13), 134106 (2014). <https://doi.org/10.1063/1.4870035>
 60. A.J. Dunnett, A.W. Chin, Simulating quantum vibronic dynamics at finite temperatures with many body wave functions at 0 K. *Front. Chem.* **8** (2021). <https://doi.org/10.3389/fchem.2020.600731>. <https://www.frontiersin.org/articles/10.3389/fchem.2020.600731>
 61. D. Tamascelli, A. Smirne, J. Lim, S.F. Huelga, M.B. Plenio, Efficient simulation of finite-temperature open quantum systems. *Phys. Rev. Lett.* **123**, 090402 (2019). <https://doi.org/10.1103/PhysRevLett.123.090402>
 62. L. Zhu, H. Liu, W. Xie, Q. Shi, Explicit system-bath correlation calculated using the hierarchical equations of motion method. *J. Chem. Phys.* **137**(19), 194106 (2012). <https://doi.org/10.1063/1.4766358>
 63. A. Chin, E. Mangaud, V. Chevet, O. Atabek, M. Desouter-Lecomte, Visualising the role of non-perturbative environment dynamics in the dissipative generation of coherent electronic motion. *Chem. Phys.* **525**, 110392 (2019). <https://doi.org/10.1016/j.chemphys.2019.110392>
 64. H.P. Breuer, F. Petruccione, *The Theory of Open Quantum Systems* (Oxford University Press, Oxford, 2002)
 65. U. Weiss, *Quantum Dissipative Systems* (World Scientific, Singapore, 2012)
 66. V. May, O. Kühn, *Charge and Energy Transfer Dynamics in Molecular Systems* (Wiley, Hoboken, 2011)
 67. A. Chenel, E. Mangaud, I. Burghardt, C. Meier, M. Desouter-Lecomte, Exciton dissociation at donor-acceptor heterojunctions: dynamics using the collective effective mode representation of the spin-boson model. *J. Chem. Phys.* **140**(4), 044104 (2014). <https://doi.org/10.1063/1.4861853>
 68. J. Iles-Smith, A.G. Dijkstra, N. Lambert, A. Nazir, Energy transfer in structured and unstructured environments: master equations beyond the Born–Markov approximations. *J. Chem. Phys.* **144**(4), 044110 (2016). <https://doi.org/10.1063/1.4940218>
 69. A. Pomyalov, C. Meier, D.J. Tannor, The importance of initial correlations in rate dynamics: a consistent non-Markovian master equation approach. *Chem. Phys.* **370**(1–3), 98–108 (2010). <https://doi.org/10.1016/j.chemphys.2010.02.017>
 70. A.G. Dijkstra, Y. Tanimura, Non-Markovian entanglement dynamics in the presence of system-bath coherence. *Phys. Rev. Lett.* **104**, 250401 (2010). <https://doi.org/10.1103/PhysRevLett.104.250401>
 71. Y. Tanimura, Reduced hierarchical equations of motion in real and imaginary time: correlated initial states and thermodynamic quantities. *J. Chem. Phys.* **141**(4), 044114 (2014). <https://doi.org/10.1063/1.4890441>
 72. L. Song, Q. Shi, Calculation of correlated initial state in the hierarchical equations of motion method using an imaginary time path integral approach. *J. Chem. Phys.* **143**(19), 194106 (2015). <https://doi.org/10.1063/1.4935799>
 73. C. Meier, D.J. Tannor, Non-Markovian evolution of the density operator in the presence of strong laser fields. *J. Chem. Phys.* **111**(8), 3365–3376 (1999). <https://doi.org/10.1063/1.4796669>
 74. S. Jang, J. Cao, R.J. Silbey, Fourth-order quantum master equation and its Markovian bath limit. *J. Chem. Phys.* **116**(7), 2705–2717 (2002). <https://doi.org/10.1063/1.1445105>
 75. E. Mulvihill, A. Schubert, X. Sun, B.D. Dunietz, E. Geva, A modified approach for simulating electronically nonadiabatic dynamics via the generalized quantum master equation. *J. Chem. Phys.* **150**(3), 034101 (2019). <https://doi.org/10.1063/1.5055756>
 76. S. Mukamel, *Principles of Nonlinear Optical Spectroscopy* (Oxford University Press, Oxford, 1995)
 77. H. Rahman, U. Kleinekathöfer, Chebyshev hierarchical equations of motion for systems with arbitrary spectral densities and temperatures. *J. Chem. Phys.* **150**(24), 244104 (2019)
 78. L. Cui, H.D. Zhang, X. Zheng, R.X. Xu, Y. Yan, Highly efficient and accurate sum-over-poles expansion of Fermi and Bose functions at near zero temperatures: Fano spectrum decomposition scheme. *J. Chem. Phys.* **151**(2), 024110 (2019)
 79. T. Ikeda, G.D. Scholes, Generalization of the hierarchical equations of motion theory for efficient calculations with arbitrary correlation functions. *J. Chem. Phys.* **152**(20), 204101 (2020). <https://doi.org/10.1063/5.0007327>
 80. Z.H. Chen, Y. Wang, X. Zheng, R.X. Xu, Y. Yan, Universal time-domain Prony fitting decomposition for optimized hierarchical quantum master equations. *J. Chem. Phys.* **156**(22), 221102 (2022). <https://doi.org/10.1063/5.0095961>

81. N. Lambert, T. Raheja, S. Cross, P. Menczel, S. Ahmed, A. Pitchford, D. Burgarth, F. Nori, QuTiP-BoFiN: a bosonic and fermionic numerical hierarchical-equations-of-motion library with applications in light-harvesting, quantum control, and single-molecule electronics (2020). <https://doi.org/10.48550/ARXIV.2010.10806>
82. U. Kleinekathöfer, Non-Markovian theories based on a decomposition of the spectral density. *J. Chem. Phys.* **121**(6), 2505–2514 (2004). <https://doi.org/10.1063/1.1770619>
83. S. Valleau, A. Eisfeld, A. Aspuru-Guzik, On the alternatives for bath correlators and spectral densities from mixed quantum-classical simulations. *J. Chem. Phys.* **137**(22), 224103 (2012). <https://doi.org/10.1063/1.4769079>
84. T. Renger, R.A. Marcus, On the relation of protein dynamics and exciton relaxation in pigment-protein complexes: an estimation of the spectral density and a theory for the calculation of optical spectra. *J. Chem. Phys.* **116**(22), 9997–10019 (2002). <https://doi.org/10.1063/1.1470200>
85. G. Ritschel, A. Eisfeld, Analytic representations of bath correlation functions for ohmic and superohmic spectral densities using simple poles. *J. Chem. Phys.* **141**(9), 094101 (2014). <https://doi.org/10.1063/1.4893931>
86. J. Hu, M. Luo, F. Jiang, R.X. Xu, Y. Yan, Padé spectrum decompositions of quantum distribution functions and optimal hierarchical equations of motion construction for quantum open systems. *J. Chem. Phys.* **134**(24), 244106 (2011). <https://doi.org/10.1063/1.3602466>
87. N. Lambert, S. Ahmed, M. Cirio, F. Nori, Modelling the ultra-strongly coupled spin-boson model with unphysical modes. *Nat. Commun.* **10**(1), 3721 (2019). <https://doi.org/10.1038/s41467-019-11656-1>
88. T.P. Fay, A simple improved low temperature correction for the hierarchical equations of motion. *J. Chem. Phys.* **157**(5), 054108 (2022). <https://doi.org/10.1063/5.0100365>
89. E. Mangaud, C. Meier, M. Desouter-Lecomte, Analysis of the non-Markovianity for electron transfer reactions in an oligothiophene-fullerene heterojunction. *Chem. Phys.* **494**, 90–102 (2017). <https://doi.org/10.1016/j.chemphys.2017.07.011>
90. R. Kubo, Stochastic Liouville equations. *J. Math. Phys.* **4**(2), 174 (1963). <https://doi.org/10.1063/1.1703941>
91. A. Ishizaki, Y. Tanimura, Quantum dynamics of system strongly coupled to low-temperature colored noise bath: reduced hierarchy equations approach. *J. Phys. Soc. Jpn.* **74**(12), 3131–3134 (2005). <https://doi.org/10.1143/JPSJ.74.3131>
92. G.C. Wick, The evaluation of the collision matrix. *Phys. Rev.* **80**, 268–272 (1950). <https://doi.org/10.1103/PhysRev.80.268>
93. H. Tamura, R. Martinazzo, M. Ruckebauer, I. Burghardt, Quantum dynamics of ultrafast charge transfer at an oligothiophene-fullerene heterojunction. *J. Chem. Phys.* **137**(22), 22A540 (2012). <https://doi.org/10.1063/1.4751486>
94. F. Di Maiolo, D. Brey, R. Binder, I. Burghardt, Quantum dynamical simulations of intra-chain exciton diffusion in an oligo (para-phenylene vinylene) chain at finite temperature. *J. Chem. Phys.* **153**(18), 184107 (2020). <https://doi.org/10.1063/5.0027588>
95. W. Popp, D. Brey, R. Binder, I. Burghardt, Quantum dynamics of exciton transport and dissociation in multichromophoric systems. *Annu. Rev. Phys. Chem.* **72**(1), 591–616 (2021). <https://doi.org/10.1146/annurev-physchem-090419-040306>
96. J. Schulze, M.F. Shibl, M.J. Al-Marri, O. Kühn, Multi-layer multi-configuration time-dependent Hartree (ML-MCTDH) approach to the correlated exciton-vibrational dynamics in the FMO complex. *J. Chem. Phys.* **144**(18), 185101 (2016). <https://doi.org/10.1063/1.4948563>
97. C. Kreisbeck, T. Kramer, A. Aspuru-Guzik, Scalable high-performance algorithm for the simulation of exciton dynamics. application to the light-harvesting complex II in the presence of resonant vibrational modes. *J. Chem. Theory Comput.* **10**(9), 4045–4054 (2014). <https://doi.org/10.1021/ct500629s>
98. R. Martinazzo, K.H. Hughes, F. Martelli, I. Burghardt, Effective spectral densities for system-environment dynamics at conical intersections: S2–S1 conical intersection in pyrazine. *Chem. Phys.* **377**(1), 21–29 (2010)
99. J. Iles-Smith, N. Lambert, A. Nazir, Environmental dynamics, correlations, and the emergence of non-canonical equilibrium states in open quantum systems. *Phys. Rev. A* **90**(3), 032114 (2014). <https://doi.org/10.1103/PhysRevA.90.032114>
100. H.P. Breuer, E.M. Laine, J. Piilo, B. Vacchini, Colloquium: non-Markovian dynamics in open quantum systems. *Rev. Mod. Phys.* **88**, 021002 (2016). <https://doi.org/10.1103/RevModPhys.88.021002>
101. I. de Vega, D. Alonso, Dynamics of non-Markovian open quantum systems. *Rev. Mod. Phys.* **89**(1), 015–001 (2017). <https://doi.org/10.1103/RevModPhys.89.015001>
102. H.P. Breuer, E.M. Laine, J. Piilo, Measure for the degree of non-Markovian behavior of quantum processes in open systems. *Phys. Rev. Lett.* **103**, 210401 (2009). <https://doi.org/10.1103/PhysRevLett.103.210401>
103. A. Rivas, S.F. Huelga, M.B. Plenio, Entanglement and non-Markovianity of quantum evolutions. *Phys. Rev. Lett.* **105**, 050403 (2010). <https://doi.org/10.1103/PhysRevLett.105.050403>
104. M.J.W. Hall, J.D. Cresser, L. Li, E. Andersson, Canonical form of master equations and characterization of non-markovianity. *Phys. Rev. A* **89**, 042,120 (2014). <https://doi.org/10.1103/PhysRevA.89.042120>. <https://link.aps.org/doi/10.1103/PhysRevA.89.042120>
105. S. Lorenzo, F. Plastina, M. Paternostro, Geometrical characterization of non-Markovianity. *Phys. Rev. A* **88**, 020102 (2013). <https://doi.org/10.1103/PhysRevA.88.020102>
106. S.C. Hou, S.L. Liang, X.X. Yi, Non-Markovianity and memory effects in quantum open systems. *Phys. Rev. A* **91**, 012109 (2015). <https://doi.org/10.1103/PhysRevA.91.012109>

107. G. Kimura, The Bloch vector for N-level systems. *Phys. Lett. A* **314**(5), 339–349 (2003). [https://doi.org/10.1016/S0375-9601\(03\)00941-1](https://doi.org/10.1016/S0375-9601(03)00941-1)
108. D. Aerts, M.S. de Bianchi, The extended Bloch representation of quantum mechanics and the hidden-measurement solution to the measurement problem. *Ann. Phys.* **351**, 975–1025 (2014). <https://doi.org/10.1016/j.aop.2014.09.020>
109. R. Puthumpally-Joseph, O. Atabek, E. Mangaud, M. Desouter-Lecomte, D. Sugny, Towards laser control of open quantum systems: memory effects. *Mol. Phys.* **115**(15–16), 1944–1954 (2017). <https://doi.org/10.1080/00268976.2017.1319085>
110. R. Puthumpally-Joseph, E. Mangaud, V. Chevet, M. Desouter-Lecomte, D. Sugny, O. Atabek, Basic mechanisms in the laser control of non-Markovian dynamics. *Phys. Rev. A* **97**, 033411 (2018). <https://doi.org/10.1103/PhysRevA.97.033411>
111. C.A. Rodríguez-Rosario, K. Modi, A. Aspuru-Guzik, Linear assignment maps for correlated system-environment states. *Phys. Rev. A* **81**, 012313 (2010). <https://doi.org/10.1103/PhysRevA.81.012313>
112. A. Brodutch, A. Datta, K. Modi, A. Rivas, C.A. Rodríguez-Rosario, Vanishing quantum discord is not necessary for completely positive maps. *Phys. Rev. A* **87**, 042301 (2013). <https://doi.org/10.1103/PhysRevA.87.042301>
113. M.D. Choi, Completely positive linear maps on complex matrices. *Linear Algebra Appl.* **10**(3), 285–290 (1975). [https://doi.org/10.1016/0024-3795\(75\)90075-0](https://doi.org/10.1016/0024-3795(75)90075-0)
114. S.H. Kye, Choi matrices revisited. *J. Math. Phys.* **63**(9), 092202 (2022). <https://doi.org/10.1063/5.0107646>
115. I.S. Dunn, R. Tempelaar, D.R. Reichman, Removing instabilities in the hierarchical equations of motion: exact and approximate projection approaches. *J. Chem. Phys.* **150**(18), 184109 (2019). <https://doi.org/10.1063/1.5092616>
116. C.P. Koch, Controlling open quantum systems: tools, achievements, and limitations. *J. Phys.: Condens. Matter* **28**(21), 213001 (2016). <https://doi.org/10.1088/0953-8984/28/21/213001>
117. B. Bylicka, D. Chruściński, S. Maniscalco, Non-Markovianity as a resource for quantum technologies (2013). <https://doi.org/10.48550/ARXIV.1301.2585>
118. N. Mirkin, P. Poggi, D. Wisniacki, Information backflow as a resource for entanglement. *Phys. Rev. A* **99**(6) (2019). <https://doi.org/10.1103/physreva.99.062327>
119. C.P. Koch, U. Boscain, T. Calarco, G. Dirr, S. Filipp, S.J. Glaser, R. Kosloff, S. Montangero, T. Schulte-Herbrüggen, D. Sugny, F.K. Wilhelm, Quantum optimal control in quantum technologies. Strategic report on current status, visions and goals for research in Europe. *EPJ Quantum Technol.* **9**(1), 19 (2022). <https://doi.org/10.1140/epjqt/s40507-022-00138-x>
120. C. Lubich, I.V. Oseledets, A projector-splitting integrator for dynamical low-rank approximation. *BIT Numer. Math.* **54**, 171–188 (2014). <https://doi.org/10.1007/s10543-013-0454-0>
121. C. Lubich, I.V. Oseledets, B. Vandereycken, Time integration of tensor trains. *SIAM J. Numer. Anal.* **53**(2), 917–941 (2015). <https://doi.org/10.1137/140976546>
122. <https://github.com/oseledets/ttpy>. Accessed 2015
123. A.J. Dunnett, A.W. Chin, Efficient bond-adaptive approach for finite-temperature open quantum dynamics using the one-site time-dependent variational principle for matrix product states. *Phys. Rev. B* **104**, 214302 (2021). <https://doi.org/10.1103/PhysRevB.104.214302>
124. S.V. Dolgov, A tensor decomposition algorithm for large odes with conservation laws. *Comput. Methods Appl. Math.* **19**(1), 23–38 (2019). <https://doi.org/10.1515/cmam-2018-0023>
125. A. Potočnik, A. Bargerbos, F.A.Y.N. Schröder, S.A. Khan, M.C. Collodo, S. Gasparinetti, Y. Salathé, C. Creatore, C. Eichler, H.E. Türeci, A.W. Chin, A. Wallraff, Studying light-harvesting models with superconducting circuits. *Nat. Commun.* **9**(1), 1–7 (2018). <https://doi.org/10.1038/s41467-018-03312-x>
126. A.W. Chin, E. Mangaud, O. Atabek, M. Desouter-Lecomte, Coherent quantum dynamics launched by incoherent relaxation in a quantum circuit simulator of a light-harvesting complex. *Phys. Rev. A* **97**, 063823 (2018). <https://doi.org/10.1103/PhysRevA.97.063823>
127. P.R. Eastham, P. Kirton, H.M. Cammack, B.W. Lovett, J. Keeling, Bath-induced coherence and the secular approximation. *Phys. Rev. A* **94**, 012110 (2016). <https://doi.org/10.1103/PhysRevA.94.012110>
128. T. Brabec, F. Krausz, Intense few-cycle laser fields: frontiers of nonlinear optics. *Rev. Mod. Phys.* **72**, 545–591 (2000). <https://doi.org/10.1103/RevModPhys.72.545>
129. D.B. Milošević, G.G. Paulus, D. Bauer, W. Becker, Above-threshold ionization by few-cycle pulses. *J. Phys. B: At. Mol. Opt. Phys.* **39**(14), R203–R262 (2006). <https://doi.org/10.1088/0953-4075/39/14/r01>
130. G.F. Thomas, Validity of the Rosen–Zener conjecture for Gaussian-modulated pulses. *Phys. Rev. A* **27**, 2744 (1983)
131. M. Holthaus, B. Just, Generalized π pulse. *Phys. Rev. A* **49**, 1950 (1994)
132. Y. Jing, L. Chen, S. Bai, Q. Shi, Equilibrium excited state and emission spectra of molecular aggregates from the hierarchical equations of motion approach. *J. Chem. Phys.* **138**(4), 045101 (2013). <https://doi.org/10.1063/1.4775843>
133. J. Ma, J. Cao, Förster resonance energy transfer, absorption and emission spectra in multichromophoric systems. I. Full cumulant expansions and system-bath entanglement. *J. Chem. Phys.* **142**(9), 094106 (2015). <https://doi.org/10.1063/1.4908599>
134. H.D. Zhang, Q. Qiao, R.X. Xu, X. Zheng, Y. Yan, Efficient steady-state solver for hierarchical quantum master equations. *J. Chem. Phys.* **147**(4), 044105 (2017). <https://doi.org/10.1063/1.4995424>
135. T. Kramer, M. Noack, A. Reinefeld, M. Rodríguez, Y. Zelinsky, Efficient calculation of open quantum system dynamics and time-resolved spectroscopy with distributed memory HEOM (DM-HEOM). *J. Comput. Chem.* **39**(22), 1779–1794 (2018). <https://doi.org/10.1002/jcc.25354>. <https://onlinelibrary.wiley.com/doi/abs/10.1002/jcc.25354>
136. H. Tamura, I. Burghardt, M. Tsukada, Exciton dissociation at thiophene/fullerene interfaces: the electronic structures and quantum dynamics. *J. Phys. Chem.*

- C **115**(20), 10205–10210 (2011). <https://doi.org/10.1021/jp203174e>
137. P.L. Walters, T.C. Allen, N. Makri, Direct determination of discrete harmonic bath parameters from molecular dynamics simulations. *J. Comput. Chem.* **38**(2), 110–115 (2017). <https://doi.org/10.1002/jcc.24527>. <https://onlinelibrary.wiley.com/doi/abs/10.1002/jcc.24527>
138. F. Häse, C. Kreisbeck, A. Aspuru-Guzik, Machine learning for quantum dynamics: deep learning of excitation energy transfer properties. *Chem. Sci.* **8**, 8419–8426 (2017). <https://doi.org/10.1039/C7SC03542J>
139. S. Bandyopadhyay, Z. Huang, K. Sun, Y. Zhao, Applications of neural networks to the simulation of dynamics of open quantum systems. *Chem. Phys.* **515**, 272–278 (2018). <https://doi.org/10.1016/j.chemphys.2018.05.019>. Ultrafast Photoinduced Processes in Polyatomic Molecules: Electronic Structure, Dynamics and Spectroscopy (Dedicated to Wolfgang Domcke on the occasion of his 70th birthday)
140. F.A.Y.N. Schröder, D.H.P. Turban, A.J. Musser, N.D.M. Hine, A.W. Chin, Tensor network simulation of multi-environmental open quantum dynamics via machine learning and entanglement renormalisation. *Nat. Commun.* **10**(1), 1–10 (2019). <https://doi.org/10.1038/s41467-019-09039-7>

Springer Nature or its licensor (e.g. a society or other partner) holds exclusive rights to this article under a publishing agreement with the author(s) or other rightsholder(s); author self-archiving of the accepted manuscript version of this article is solely governed by the terms of such publishing agreement and applicable law.